

## DISEASES AND DISORDERS

# Epigenetic reprogramming driving successful and failed repair in acute kidney injury

Yoshiharu Muto<sup>1</sup>, Eryn E. Dixon<sup>1</sup>, Yasuhiro Yoshimura<sup>1</sup>, Nicolas Ledru<sup>1</sup>, Yuhei Kirita<sup>1</sup>, Haojia Wu<sup>1</sup>, Benjamin D. Humphreys<sup>1,2,\*</sup>

Acute kidney injury (AKI) causes epithelial damage followed by subsequent repair. While successful repair restores kidney function, this process is often incomplete and can lead to chronic kidney disease (CKD) in a process called failed repair. To better understand the epigenetic reprogramming driving this AKI-to-CKD transition, we generated a single-nucleus multiomic atlas for the full mouse AKI time course, consisting of ~280,000 single-nucleus transcriptomes and epigenomes. We reveal cell-specific dynamic alterations in gene regulatory landscapes reflecting, especially, activation of proinflammatory pathways. We further generated single-nucleus multiomic data from four human AKI samples including validation by genome-wide identification of nuclear factor  $\kappa$ B binding sites. A regularized regression analysis identifies key regulators involved in both successful and failed repair cell fate, identifying the transcription factor CREB5 as a regulator of both successful and failed tubular repair that also drives proximal tubular cell proliferation after injury. Our interspecies multiomic approach provides a foundation to comprehensively understand cell states in AKI.

## INTRODUCTION

Acute kidney injury (AKI) is characterized by a sudden decrease in renal function, usually from ischemic or toxic insults (1, 2). AKI is very common especially among hospitalized patients with an incidence up to ~15% and approaching ~50% among critically ill elderly patients (2). AKI causes short-term morbidity and mortality, but it also presents substantial risk of the development of future chronic kidney diseases (CKDs), termed the AKI-to-CKD transition (1–3). Several lines of evidence have demonstrated that the AKI-to-CKD transition involves inflammation driving subsequent interstitial fibrosis (3). Tubular cell injury causes proinflammatory changes that promotes an innate immune response through recruitment and activation of immune cells, further promoting local inflammation (3). Both resident macrophages and infiltrating monocytes differentiate into distinct proinflammatory or profibrotic subsets depending on microenvironmental cues and contribute to remodeling in the microenvironment (4, 5). Proinflammatory and profibrotic mediators activate other interstitial cell types, leading to loss of parenchyma and irreversible interstitial fibrosis, the final and common pathway in CKD (6). The molecular mechanisms underlying both successful kidney repair and the AKI-to-CKD transition remain incompletely understood. During AKI and subsequent repair, the epigenetic dynamics across diverse kidney cell types are especially poorly described because, until recently, methods to characterize these cell-specific changes were unavailable. Deciphering epigenetic changes during injury and repair will be important to identify previously unrecognized therapeutic targets for intervention (7).

We and others have generated single-nucleus transcriptomic atlases from mouse kidneys after ischemia-reperfusion injury (IRI) and identified a *Vcam1*-expressing subset of proximal tubular cells (PTCs) that emerges and persists after kidney injury (8–10). This cell state is characterized by a unique proinflammatory gene

expression signature, and it persists later after injury, leading us to name it failed repair PTCs (FR-PTCs) (8, 9, 11). Furthermore, similar PTC subtype expressing vascular cell adhesion molecule 1 (VCAM1) was also observed in healthy and CKD human kidneys (12–14). The frequency of FR-PTCs in advanced human CKD due to autosomal dominant polycystic kidney disease (ADPKD) was also markedly increased, replacing normal PTCs (13). The increase in FR-PTCs in CKD suggests a potential causative role in the AKI-to-CKD transition and CKD progression broadly. However, the molecular mechanisms driving a failed repair gene expression signature and a role in interstitial fibrosis driving CKD progression are incompletely understood.

Epigenomic alterations have recently gained attention as drivers of the AKI-to-CKD transition (15–17). Previously, we have defined cell type-specific epigenetic signatures in healthy (12) and ADPKD and CKD (13, 14) human kidneys, highlighting the enrichment of nuclear factor  $\kappa$ B (NF- $\kappa$ B) transcription factor (TF) binding sites on accessible chromatin regions in FR-PTCs. We have interpreted increased chromatin accessibility for NF- $\kappa$ B binding motifs in the FR-PTC state as reflecting a central role for this proinflammatory TF in promoting inflammation, fibrosis, and the AKI-to-CKD transition. Consistent with this, Gerhardt et al. (11) recently performed a single-nucleus multiomic analysis on genetically labeled *Ki67*<sup>+</sup> cells at two time points after IRI (4 weeks and 6 months), describing proinflammatory transcriptomic and epigenetic alterations in *Vcam1*<sup>+</sup> FR-PTCs even 6 months after the insult, suggesting persistent epigenetic alterations after tubular injury. The lack of comprehensive, cell type-specific epigenomic analysis along multiple time points from the acute to chronic phase of AKI hampers our understanding of the epigenetic mechanisms driving the FR-PTC state.

Here, we performed single-nucleus ATAC sequencing (snATAC-seq) on mouse kidneys following IRI to comprehensively describe the cell-specific epigenetic states and temporal dynamics in the AKI-to-CKD transition. This single-nucleus epigenetic atlas was integratively analyzed with single-nucleus RNA sequencing (snRNA-seq) data from the same samples (8), and we describe the cis-regulatory epigenetic network driving failed repair cell states. To validate our

Copyright © 2024 The Authors, some rights reserved; exclusive licensee American Association for the Advancement of Science. No claim to original U.S. Government Works. Distributed under a Creative Commons Attribution NonCommercial License 4.0 (CC BY-NC).

<sup>1</sup>Division of Nephrology, Department of Medicine, Washington University in St. Louis, St. Louis, MO, USA. <sup>2</sup>Department of Developmental Biology, Washington University in St. Louis, St. Louis, MO, USA.

\*Corresponding author. Email: humphreysbd@wustl.edu

findings for mouse kidneys with IRI, we further generated paired multimodal single-nucleus multiomic datasets from four human AKI kidney samples. Interspecies multimodal analysis identified cyclic adenosine monophosphate (cAMP) response element-binding protein 5 (CREB5) as a critical TF potentially involved in both the recovery and failed repair processes in PTCs. We also generated an interactive data visualization tool for single-nucleus epigenomic data (<http://humphreyslab.com/SingleCell/>). This detailed temporal single-nucleus multiomic atlas mouse kidney IRI reveals the comprehensive cell-specific epigenetic landscape during the IRI disease course and provides a foundation to better understand disease mechanisms.

## RESULTS

### Single-nucleus chromatin accessibility atlas for mouse kidneys with IRI

We performed snATAC-seq on a total of 19 male mouse kidney samples collected along six time points (sham, 4 and 12 hours, and 2, 14, and 42 days after bilateral IRI;  $n = 3$  to 4 per time point) with 10X Genomics Chromium Single Cell ATAC v1 (Fig. 1A). The snRNA-seq for these samples was previously reported (8). After batch quality control (QC) filtering and preprocessing (see also Materials and Methods), label transfer (Seurat) was performed on the snATAC-seq dataset using the snRNA-seq dataset (18, 19). The snATAC-seq datasets were filtered using a 60% confidence threshold for cell type assignment to remove heterotypic doublets (fig. S1A). Nuclei with inconsistent annotations between label transfer and manual annotation based on known cell type marker gene activities were further removed as remaining doublets and low-quality nuclei (fig. S1, B to F; see also Materials and Methods). The resultant datasets with high-quality nuclei were integrated with Harmony (20) and visualized in Uniform Manifold Approximation and Projection (UMAP) space (Fig. 1B). We detected 193,731 accessible chromatin regions ( $7906 \pm 4286$  regions per nucleus) among 157,000 nuclei in the final dataset. The differentially accessible regions (DARs) in each cluster include the transcription start site (TSS) of known cell type marker genes (Fig. 1C and data S1), confirming our cell type annotations. Gene activities were predicted by accessibility of a gene body and promoter and used to further confirm our cell type annotations (fig. S2). The QC metrics of snATAC-seq fragments in each time point indicated that the quality of samples during the time course following ischemic injury was maintained (fig. S3, A to C). The QC metrics among cell types indicate that proximal convoluted and straight tubules (PCTs/PSTs) have the best quality (fig. S3, D to F), although other cell types also showed sufficient quality to evaluate the DARs (Fig. 1C and data S1) and TF motif enrichment in accessible regions (data S2).

### Mouse PTC heterogeneity after IRI

We have previously identified FR-PTCs that emerge after IRI, adopt a proinflammatory and profibrotic phenotype, and persist in mouse kidneys (8). To better understand the epigenetic mechanism driving successful and failed repair of PTCs, we subclustered PCT/PST clusters (Fig. 2A), identifying PTC subtypes with mild-to-severe injury and the FR-PTC state, which, as expected, had specifically increased accessibility to the *Vcam1* gene promoter (Fig. 2B and data S3). The injured PTC subtypes display accessibility to the promoter of *Krt20*, previously found to be expressed in injured PTCs in mouse kidneys

(21). Gene expression signatures in the snRNA-seq dataset (fig. S4A) (8) were similar to gene activities predicted from accessibility of a promoter and gene body (fig. S4B) among PTC subtypes, confirming our PTC subtype annotation. TF motif enrichment analysis with chromVAR (22) identified PTC subtype-specific TF motif enrichment on open chromatin regions (Fig. 2C and data S4). The Hepatocyte nuclear factor 4 $\alpha$  (HNF4A) binding motif was enriched in healthy PTC subtypes, and this was lost in injured and failed repair cell states, consistent with previous findings in human kidneys (12). In contrast, motif enrichment for an activating protein 1 (AP-1) family TF JUN/FOS and nuclear factor erythroid 2-related factor 2 (NFE2L2) was observed widely among injured PTC states along the time course (Fig. 2D and fig. S5A). NFE2L2 regulates the expression of a cohort of antioxidant genes, protecting against oxidative stress induced by IRI and other renal insults (23). FR-PTCs had enhanced NFE2L2 motif availability compared to healthy PTCs, suggesting a sustained oxidative stress response in FR-PTCs (fig. S5A). However, the similar pattern of motif enrichment between JUN/FOS and NFE2L2 may simply reflect their indistinguishable consensus sequences (24) on the open chromatin regions rather than true binding of the TFs, warranting a future validation study. The binding motifs for NF- $\kappa$ B family TFs were most enriched in FR-PTCs (Fig. 2D), in agreement with previous findings in mouse and human kidneys (8, 11, 12). Together, these findings reveal distinct epigenetic programs between different PTC states after injury, likely reflecting separate gene regulatory networks.

The S3 segment is the most vulnerable to IRI among PTCs in most animal models of ischemia (25). To further characterize epigenetic response following acute tubular injury, we evaluated the motif enrichment signature of the injured S3 segment over time (Fig. 2E) (8). Of note, in healthy S3 PTCs, the TF motif enrichment signatures were not completely recovered 6 weeks after IRI, consistent with the recent finding that transcriptional and epigenetic alteration in adaptive PTCs persists for a long period, even 6 months after IRI (11). The S3 segment at day 2 was specifically enriched in NF- $\kappa$ B TF motif availability and the Hippo pathway effector TEA domain family member (TEAD) molecules and the CCCTC-binding factor (CTCF) motif. The specific enrichment of the NF- $\kappa$ B motif is consistent with our previous observation that PTCs expressing VCAM1 emerge in the Hepatitis A virus cellular receptor 1 (HAVCR1)-positive injured tubules in a scattered manner at day 2 following IRI (8). CTCF is a multifunctional TF serving as an architectural protein to create boundaries between topologically associating domains in chromosomes, regulating interactions between cis-regulatory regions (CREs) and promoters (26). A previous study has shown that ~60% of CTCF binding sites are cell type-specific (26), suggesting that reorganization of CTCF availability may reflect global epigenomic remodeling in the injured S3 segment. To assess the cell fate of the injured S3 segment at day 2, we constructed a pseudotemporal trajectory (27) on the S3 segment population with injury (Injured S3: days 2 and 14) and recovery (Healthy S3: days 14 and 42) and PTCs with failed recovery (FR-PTCs: days 14 and 42) (Fig. 2F). The injured S3 segment at day 2 has two separate fates—either to healthy PTCs or to the failed repair cell state. Given the transient activation of the NF- $\kappa$ B binding motif in the injured S3 segment at day 2 (Fig. 2E) and following its persistent activation in FR-PTCs (Fig. 2D), NF- $\kappa$ B activation may initiate and promote the failed repair branch of the trajectory (Fig. 2F).

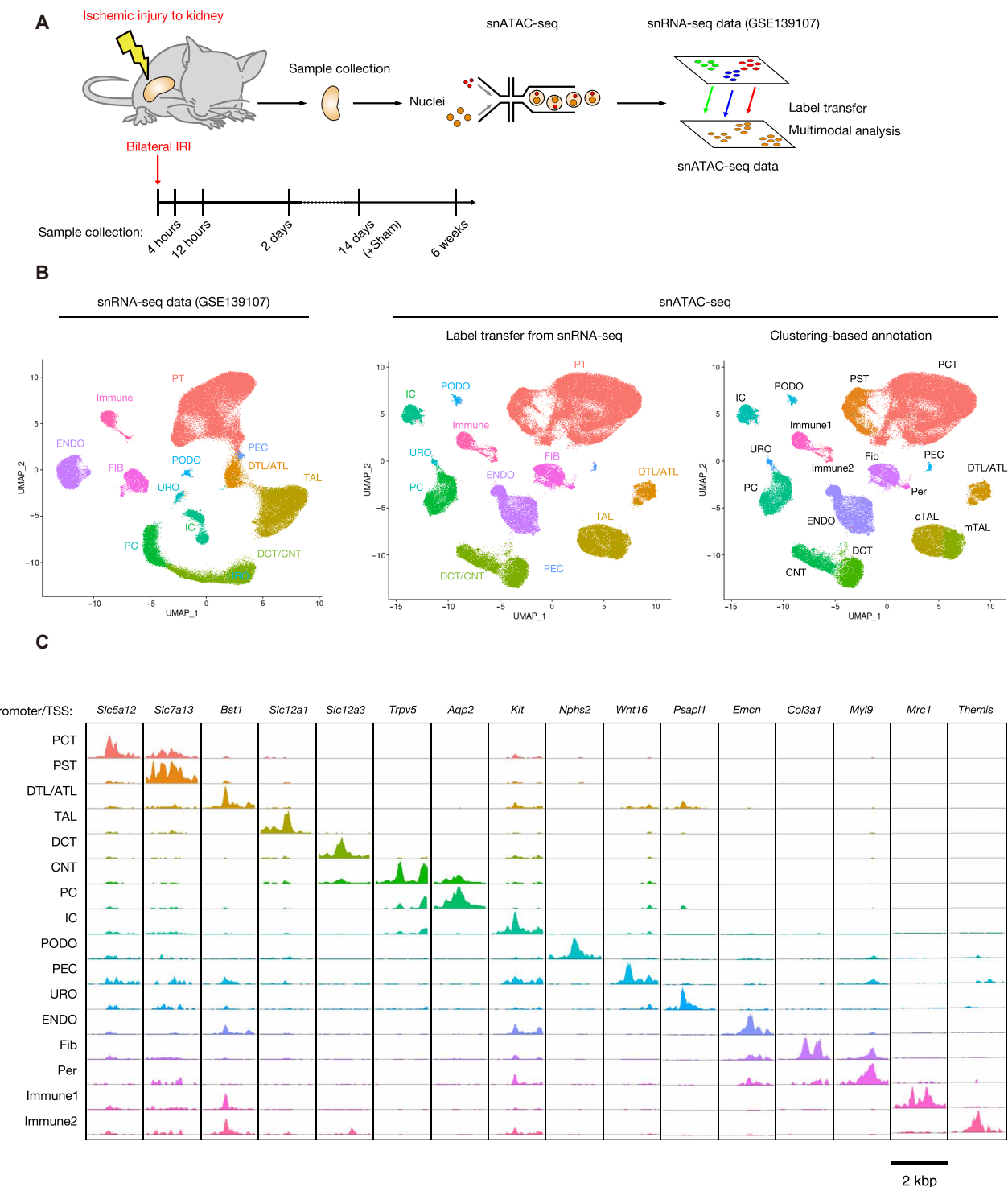


**Fig. 1. Single-nucleus epigenetic profiling for mouse kidneys with IRI along the time course.** (A) Overview of experimental methodology. Single-nucleus chromatin accessibility atlas was generated from mouse kidneys along the time course after bilateral IRI ( $n = 3$  to 4 for each time point) and analyzed together with the previously generated snRNA-seq dataset. (B) UMAP plot of the previously generated snRNA-seq dataset (left) and newly sequenced snATAC-seq dataset with annotation by label transfer from the snRNA-seq dataset (middle) and clustering-based annotation (right). PT, proximal tubule; PCT, proximal convoluted tubule; PST, proximal straight tubule; PEC, parietal epithelial cells; DTL/ATL, descending/ascending thin limb of Henle's loop; cTAL/mTAL, cortical/medullary thick ascending limb of Henle's loop; DCT, distal convoluted tubule; CNT, connecting tubule; PC, principal cells; ICA, type A intercalated cells; ICB, type B intercalated cells; PODO, podocytes; ENDO, endothelial cells; FIB (Fib), fibroblasts; Per, pericytes; Immune, immune cells; URO, uroepithelium. Clustering for snRNA-seq data was performed in our previous study (8). (C) Fragment coverage (frequency of Tn5 insertion) around the DARs around each cell type at lineage marker gene TSSs. Scale bar, 2 kbp.

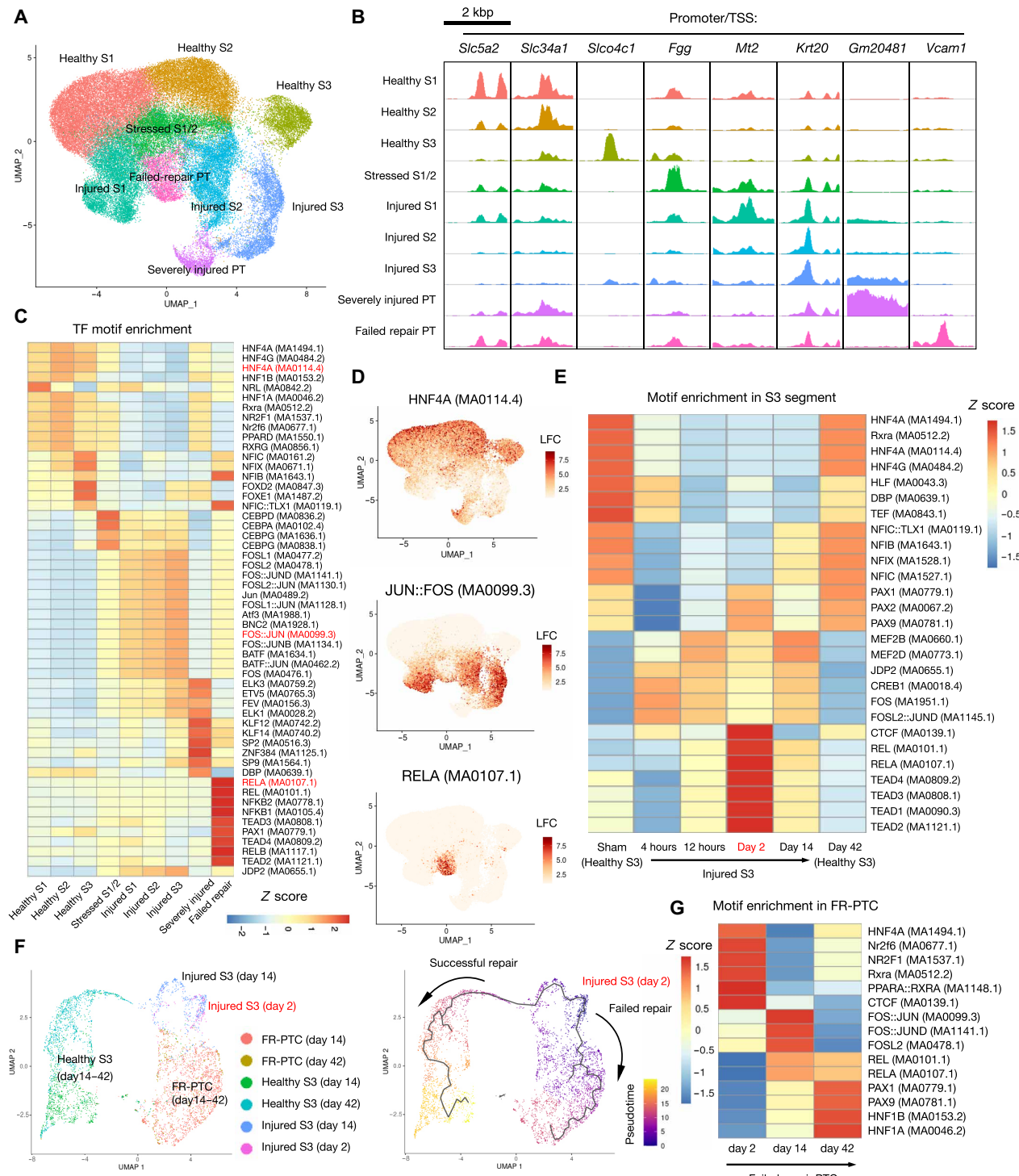


**Fig. 2. Heterogeneity of mouse PTCs following IRI.** (A) Subclustering of snATAC-seq PCTs/PSTs on the UMAP plot with annotations by subtypes. (B) Fragment coverage around the TSS of DARs in each subtype. Scale bar, 2 kbp. (C) Heatmap showing relative TF motif enrichment in each PTC subtype. The most enriched motifs in each subtype are shown. (D) UMAP plot showing the chromVAR motif enrichment score in PTCs for HNF4A (MA0114.4, top), JUN:FOS (MA0099.3, middle), and RELA (MA0107.1, bottom). The color scale for each plot represents a normalized log(fold change) (LFC) for the respective assay. (E) Heatmap showing the relative motif enrichment for Healthy S3 in sham and 42 days after IRI, Injured S3 at 4 and 12 hours, and 2 and 14 days after IRI. The most enriched motifs among injured S3 time points (4 and 12 hours and 2 and 14 days after IRI) are shown. (F) Pseudotemporal trajectory to model the successful and failed recovery of injured PTC S3 segment cells, constructed with injured S3 cluster at day 2/day 14, Healthy S3 cluster day 14/day 42 (successful recovery), and FR-PTCs at day 14/day 42 (failed recovery) following IRI. Colored by the subtypes (left) or pseudotime (right). (G) Heatmap showing the relative motif enrichment for FR-PTCs at 2/14/42 days after IRI. The most enriched motifs in each time point are shown.

NF- $\kappa$ B activation in FR-PTCs was most prominent at day 14 and decreased at day 42 (Fig. 2G), although NF- $\kappa$ B activation was still prominent compared to other cell states at day 42 (fig. S6). AP-1 TF motif enrichment observed at day 14 was also diminished at day 42 (Fig. 2G), indicating resolution of acute inflammation. In contrast, paired-box (PAX) family TF motif enrichment was increased in FR-PTCs at day 42 compared to day 14 (Fig. 2G). Among PAX family genes, *Pax8* expression was relatively abundant in FR-PTCs compared to healthy subtypes at day 42 after IRI in snRNA-seq (fig. S7), although the *Pax8* expression level was the highest among injured PTC S3 segments in the whole dataset (fig. S7). *PAX8* was recently found to promote renal cell carcinoma (28, 29), which was also shown to differentiate from VCAM1+ PTCs (30). This finding suggests that *PAX8* may contribute to an FR-PTC gene expression signature at the later stage of the time course after IRI. These analyses on PTCs collectively indicate that temporal dynamics of cell type-specific TF activation is associated with tubular injury and recovery after IRI and that NF- $\kappa$ B is potentially involved in the determination of PTC fate after injury.

### Genome-wide proximal tubular RELA binding sites

Our motif enrichment analysis on mouse PTCs following IRI (Fig. 2) and previous findings (8, 11–14) indicates activation of the NF- $\kappa$ B pathway in FR-PTCs. The accessibility of TF binding motifs allows for prediction of TF activity (22), but it represents an inference and not an actual measurement of TF-DNA interaction. To validate these predictions, we used cleavage under targets and release using nuclease (CUT&RUN) to directly identify genome-wide v-rel avian reticuloendotheliosis viral oncogene homolog A (RELA) binding sites in primary human PTCs (31). To authenticate primary human PTCs to study the AKI-to-CKD transition, we performed deconvolution analysis on the bulk RNA-seq data for primary human PTCs with the mouse IRI data using CIBERSORTx, a machine learning method that imputes gene expression profiles and estimates the frequency of cell types in a mixed cell population (32). The deconvolution analysis predicted that a large part (~50%) of primary renal proximal tubular epithelial cells (RPTECs) showed the gene expression signature of injured PTCs (fig. S8A), consistent with their proliferative capacity. A total of ~30% of primary culture cells were predicted to demonstrate the FR-PTC gene expression signature (fig. S8A), and the predicted FR-PTC frequency decreased after small interfering RNA (siRNA) knockdown of NFAT5—one of the regulators for the failed repair cell state identified in our previous study (fig. S8, B and C) (33). These analyses indicate that the human primary PTC culture can be a model of injured PTCs potentially transitioning to FR-PTCs.

We detected RELA binding to genomic DNA in primary human PTCs after tumor necrosis factor- $\alpha$  (TNF $\alpha$ ) treatment (Fig. 3A), which activates the canonical NF- $\kappa$ B pathway (34). We identified 2004 RELA binding peaks (data S5), which include both genomic regions with the H3K4me3+ promoter mark and those with H3K-4me3-/H3K27ac+ enhancer marks (Fig. 3A). Genes whose TSS was located close to RELA binding sites (within 2 kbp from the TSS) were enriched with the genes of I- $\kappa$ B/NF- $\kappa$ B complex [fold enrichment: 64.55 and false discovery rate (FDR) = 0.00088; Fig. 3B and data S6] among cellular component gene ontology (GO) terms and NIK (NF- $\kappa$ B-inducing kinase)—NF- $\kappa$ B signaling (fold enrichment: 12.01 and FDR = 0.00017; data S7) among biological process GO

terms. The RELA binding peaks were located in promoter regions within 2 kbp from the TSS (20.8%), introns (44.5%), and distal intergenic regions (28.7%; Fig. 3C), broadly covering both promoters and enhancers. Next, we asked which mouse FR-PTC DARs contain conserved RELA binding sites. We lifted human RELA binding peaks to the mm10 mouse genome (minimum ratio of bases that must remap: 0.1, 1438 peaks, and recovery rate: 71.7%) (35). The lifted RELA binding sites were intersected with mouse FR-PTC DARs (Fig. 3D and data S3), identifying 103 conserved RELA binding sites in FR-PTC DARs (data S8). The nearby genes of those DARs were enriched with chemokine activity (fold enrichment: 28.4 and FDR = 0.034) (Fig. 3E and data S9), suggesting that NF- $\kappa$ B activation in FR-PTCs may promote local inflammation through chemokine secretion.

Among secretory molecules expressed in FR-PTCs, *Ccl2* expression is prominently up-regulated (Fig. 4A) (9, 11). C-C motif chemokine ligand 2 (CCL2) is a proinflammatory cytokine that has been implicated in AKI pathogenesis by recruiting immune cells to the local injured tubules (36, 37). To characterize epigenetic mechanisms driving *Ccl2* up-regulation in FR-PTCs, we constructed a cis-coaccessibility network (CCAN) (27) in FR-PTCs around the *Ccl2* locus (Fig. 4, B and C). A DAR with a conserved RELA binding site located at ~2 kbp upstream of the *Ccl2* TSS (Fig. 4B) was predicted to interact with the TSS, suggesting that this CRE may activate *Ccl2* expression in a RELA-dependent manner in FR-PTCs. Similarly, a total of five DARs with RELA binding sites were observed in the intron and 5' distal region (within 100 kbp) of the *Csf1* gene. Among them, the DAR at 30 kbp upstream was predicted to strongly interact with the TSS of *Csf1* (Fig. 4D). *Csf1* encodes macrophage colony-stimulating factor (M-CSF or CSF1), a growth factor for monocyte/macrophage lineage and a major regulator of their proliferation and differentiation (38). Previous lines of evidence have shown the roles of CSF1 in tubular epithelial regeneration by expansion and M2 polarization of resident macrophages in the short term after renal injury (39–41), although, in other contexts, CSF1 expression can be detrimental, promoting tissue fibrosis (42, 43). *Csf1* was up-regulated in injured PTCs and FR-PTCs (Fig. 4A), in agreement with the previous literature (39, 41). These results are consistent with the notion that RELA regulates the expression of proinflammatory molecules through CREs.

Genes up-regulated in FR-PTCs with conserved RELA binding sites in DARs also included nonsecretory, membrane-bound signaling molecules involved in local inflammation. For example, *Cd47*, which encodes a membrane protein suppressing macrophage-mediated phagocytosis by sending a “do not eat me” signal through interaction with signal regulatory protein  $\alpha$  (SIRPa) (44). *Cd47* expression was up-regulated in FR-PTCs (fig. S9A), suggesting a potential mechanism for the persistence of the FR-PTCs for a prolonged period after the injury. The RELA binding DAR located 3' distal to the *Cd47* gene was predicted to interact with accessible regions near the TSS (fig. S9B).

We overlaid CTCF chromatin immunoprecipitation sequencing (ChIP-seq) track for an adult mouse kidney (35, 45) onto the CCAN (fig. S10, A to C). The nearest CTCF peaks to the potential CRE (fig. S10A) demarcated the CCAN (Fig. 4C) in the *Ccl2* gene. We also observed that the coaccessibilities were often modeled beyond CTCF peaks. For example, a few coaccessibilities from 5' distal CRE to 3' distal CRE around *Csf1* were predicted beyond the intronic CTCF peak (fig. S10B). The CTCF binding sites we used were for a bulk mouse kidney, and CTCF may not bind this intronic region in

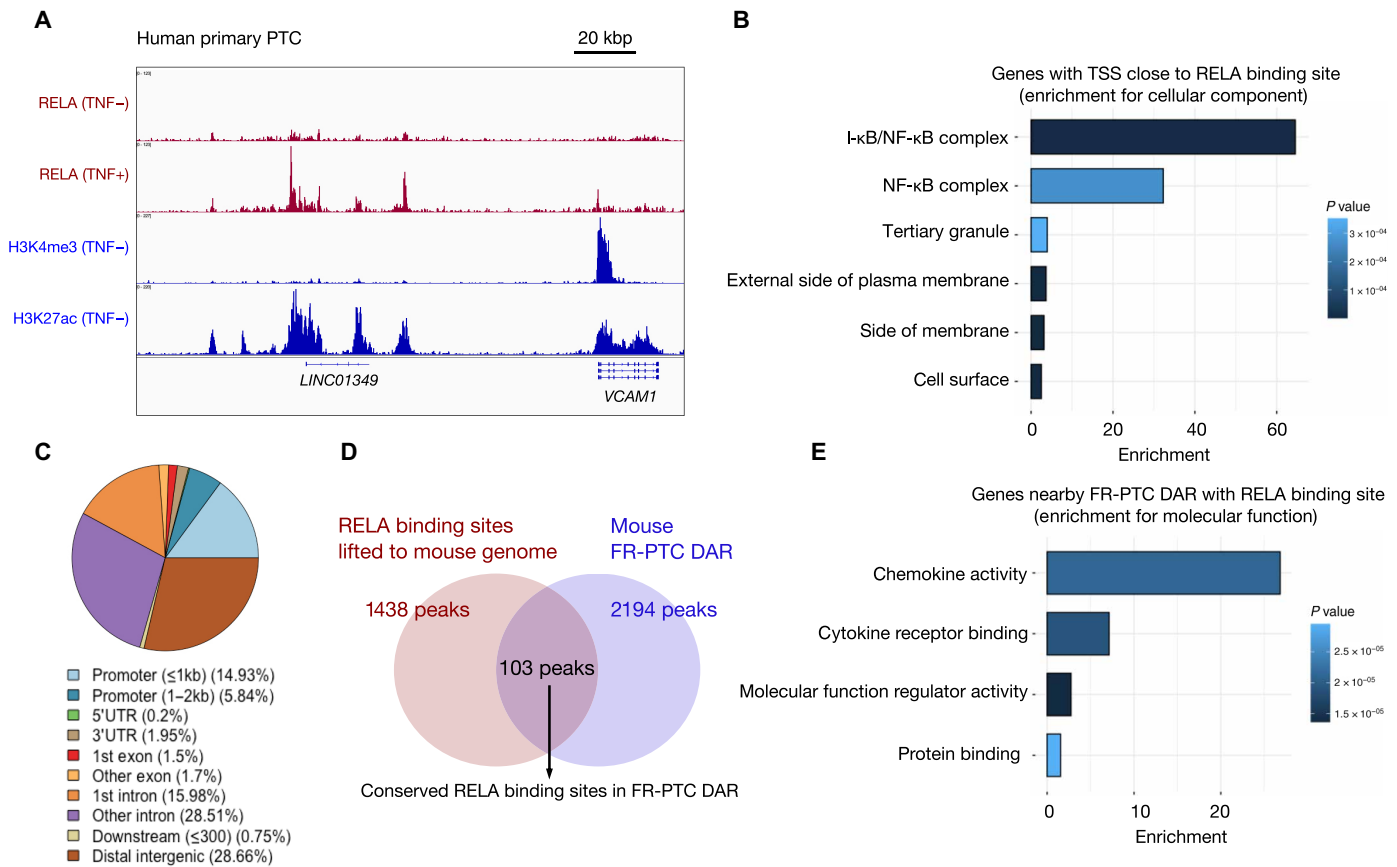


**Fig. 3. Genome-wide proximal tubular RELA binding sites.** (A) RELA binding sites with or without TNF $\alpha$  treatment (100 ng/ml, top) and histone methylation and acetylation (without TNF $\alpha$  treatment, bottom) around the VCAM1 gene in human primary PTCs determined by the CUT&RUN assay. Scale bar, 20 kbp. (B) Cellular component GO term enrichment analysis for the human genes with the TSS close to RELA binding sites ( $<2$  kbp). The six most enriched terms are shown. The color scale for each bar represents a P value. (C) Pie chart of annotated RELA binding site locations. 5'UTR, 5' untranslated region; 3'UTR, 3' untranslated region. (D) RELA binding peaks lifted to the mm10 mouse genome were intersected with murine FR-PTC DARs, identifying 103 conserved RELA binding sites in FR-PTC DARs. (E) Molecular function GO term enrichment analysis for the nearby mouse genes of conserved RELA binding sites in the murine FR-PTC DARs. The color scale for each bar represents a P value.

FR-PTCs. CTCF motif availability was dynamically altered in PTCs during a time course after IRI (Fig. 2E).

We next investigated if the TNF $\alpha$ -induced expression of a subset of these genes was directly regulated by either RELA or v-rel avian reticuloendotheliosis viral oncogene homolog B (RELB) by siRNA knockdown in human PTCs. The expression of these genes (*CCL2*, *CSF1*, and *CD47*) predicted to interact with RELA in mouse FR-PTCs was up-regulated by TNF $\alpha$  treatment (Fig. 4E and fig. S9, C to E), although the extent to which *RELA* contributes to their gene expression level was variable (Fig. 4E and fig. S9E). *CCL2* expression was highly dependent on *RELA* regardless of TNF $\alpha$  treatment. The noncanonical NF- $\kappa$ B regulator *RELB* also regulated *CCL2* expression, although its regulation is more dependent on *RELA*. Of note, *RELB* expression was also regulated by *RELA* in TNF $\alpha$ -treated cells (fig. S9D). *CSF1* expression is also regulated by *RELA* in a TNF $\alpha$ -dependent manner. In contrast, the role of *RELA* in *CD47* expression was limited in human primary PTCs (fig. S9E). Concurrent binding of other transcriptions may be needed for *RELA* to fully activate *CD47* expression. These findings collectively suggest that the FR-PTC proinflammatory gene expression signature is shaped by numerous CREs; many but not all of which require NF- $\kappa$ B signaling.

### Immune cells potentially regulated by FR-PTCs

Given epigenetic alterations driving the expression of various cytokines and other membrane-bound signaling molecules interacting with immune cells in injured and FR-PTCs (Fig. 4 and fig. S9), transcriptional and epigenetic remodeling of immune cells may be coordinately regulated by PTCs during AKI. Immune cells clustered into six cell types in our snRNA-seq dataset (fig. S11, A and B), as described in our previous work (8). Three subtypes are macrophages expressing *Mrc1* (fig. S11, A and B), which encodes a mannose receptor protein and marks alternatively activated macrophages (M2 macrophage) in both humans and mice (4, 5). We also observed *Flt3*-expressing dendritic cells (DCs), T cells with *themis* expression, and B cells with *Cd19* expression. Each of the three *Mrc1*+ macrophage subtypes expressed unique markers (*Itga9*, *Plcb1*, and *Gpnmb*). Among them, *CCL2* receptor gene *Ccr2* was mainly expressed in *Plcb1*+ macrophage (*Plcb1*+Mac), and *CSF1* receptor gene *Csf1r* was mainly detected in *Itga9*+Mac, suggesting that FR-PTCs may interact with heterogeneous macrophage subtypes (fig. S11C) through distinct subsets of secretory molecules. *Sirpa* coding SIRP $\alpha$  protein, which receives the signal from CD47 to prevent phagocytosis, is expressed in *Plcb1*+Mac (fig. S11D). FR-PTCs

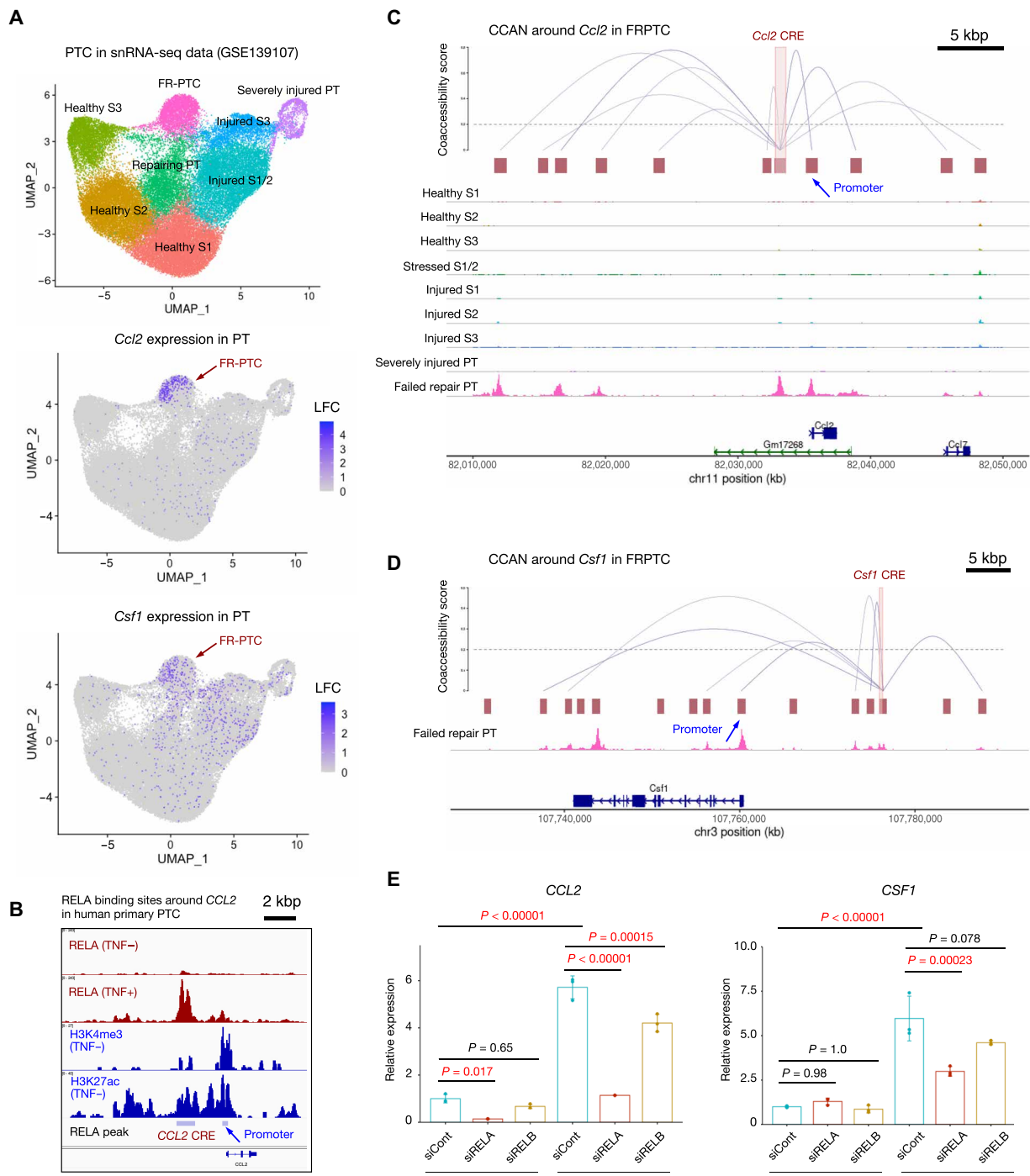


**Fig. 4. Cis-regulatory network driving inflammation by NF- $\kappa$ B signaling in failed repair cells.** (A) UMAP plot showing cell annotations (top) and a gene expression level of *Ccl2* (middle) and *Csf1* (bottom) among mouse PTC subtypes. The color scale for each plot represents a normalized LFC for the respective assay. Subclustering and cell type annotation were performed and shown in our previous study (8). (B) RELA binding site near the *CCL2* gene identified by the CUT&RUN assay for primary RPTECs treated with or without TNF $\alpha$  treatment (100 ng/ml, top). CUT&RUN assay peaks for H3K4me3 and H3K27ac in primary RPTECs without TNF $\alpha$  treatment (middle) and RELA binding peaks (bottom) are also shown. Scale bar, 2 kbp. (C) CCAN predicts interactions (gray arcs) of a CRE with a conserved RELA binding site (chr11:82032734-82033526) and other accessible regions (red boxes) near the *Ccl2* gene in the mouse FR-PTCs are shown (top). Coverage plot showing accessible regions in each PTC subtypes are also shown (bottom). The y axis is the cis-coaccessibility score, and a higher number indicates higher coaccessibility. Scale bar, 5 kbp. (D) Predicted interactions of a CRE with a conserved RELA binding site (chr3: 107,775,891 to 107,776,242) and other accessible regions in the mouse FR-PTCs (top) around the *Csf1* gene in the mouse kidneys. Chromatin accessibility in FR-PTCs determined by snATAC-seq is also shown (bottom). Scale bar, 5 kbp. (E) qPCR for *CCL2* or *CSF1* expression levels in primary human PTCs with siRNA knockdown of *RELA* or *RELB* treated with or without TNF $\alpha$  (100 ng/ml) treatment. NT, no treatment.  $n = 3$  biological replicates. Bar graphs represent the mean, and error bars are the SD. One-way ANOVA with post hoc Tukey test.

recruit and activate *Plcb1*+Mac by CCL2, although they may inhibit their phagocytosis through CD47-SIRP $\alpha$  interaction.

To better understand macrophage heterogeneity in mouse kidney IRI, we subclustered immune cell clusters (Immune1 and Immune2) from our snATAC-seq data, identifying eight subtypes (fig. S12, A to C, and data S10). The number and composition of these immune cell subtypes were dynamically increased immediately after IRI (fig. S12B), and this increase persisted at 6 weeks after IRI, suggesting potential roles in the long-term tissue remodeling and the AKI-to-CKD transition. Integration and label transfer from snRNA-seq data suggested robust identification of T cells, B cells, DCs, and *Itga9*+Mac (fig. S12D, E). In contrast, *Plcb1*+Mac and *Gpnmb*+Mac prediction was weak, likely reflecting low numbers of immune cell nuclei. Nevertheless, the TSS of *Plcb1* was specifically accessible in Mac5 subtypes (fig. S12C), suggesting that Mac5 is the *Plcb1*-expressing macrophage. We observed M1 macrophage with specific accessibility to the *Cd80* TSS without *Mrc1* accessibility only in snATAC-seq (fig. S12C), potentially due to a low *Cd80* expression level. Mac2, 3, and 4 subtypes displayed accessibility of the TSS in *Itga9* and *Mrc1* genes, suggesting that they are *Itga9*+ macrophage (fig. S12C). The accessibility of the *Ccr2* TSS was observed broadly among immune cells except B cells, although the accessibility was most notable in Mac4, consistent with a high *Ccr2* expression level in *Plcb1*+Mac in snRNA-seq data. The gene activities predicted by snATAC-seq also suggested that Mac1 as M1 macrophage (*Il1b*, *Cd80*, and *Nos2*) and that Mac2–5 subtypes were with M2 activation (*Mrc1* and *Cd86*; fig. S12F). M2 macrophage was previously shown to contribute to tissue repair and tissue fibrosis through transforming growth factor- $\beta$  (TGF $\beta$ ) signaling (5). *Tgfb1* gene activity was predicted to be increased in Mac2–5 (fig. S12F). We next performed TF motif enrichment analysis in macrophage subtypes (fig. S13A and data S11). The resident macrophage subtype (Mac2) showed increased availability of the mineral corticoid receptor NR3C2 binding motif compared to other macrophage subtypes (fig. S13A) after renal injury (4 hours and 2 days; fig. S13B), consistent with the previous literature implicating mineral corticoid activity on the myeloid cells in renal fibrosis following kidney IRI (46, 47). The most enriched motifs in *Ccr2*+ macrophage (Mac5) were AP-1 family TFs FOSL1 and JUN (fig. S13A) that were activated immediately following IRI (fig. S13C), likely reflecting numerous proinflammatory microenvironmental signals. These findings collectively suggest that FR-PTCs interact with various immune cell subsets by sending molecular cues, contributing to the macrophage heterogeneity following IRI.

### PTC heterogeneity in human AKI

To extend our multiomic atlas of mouse IRI, we next generated paired snRNA-seq and snATAC-seq datasets on the four kidney cortex samples of the patients with AKI due to ischemic acute tubular necrosis (ATN;  $n = 3$ ) or undetermined cause ( $n = 1$ , associated with pneumonia) (data S12). The diagnosis of ischemic ATN came from the fact that the patients were all found down, and they underwent a variable length (25 to 45 min) of cardiopulmonary resuscitation. The AKI kidney samples were procured postmortem, so the kidneys were exposed to an additional hypoperfusion-hypoxic period, which might further induce and deteriorate ischemic ATN. Although we adopted different protocols of procurement between two groups (healthy: nephrectomy and AKI: postmortem), we expect that the influence of the postmortem procurement on our

AKI samples is in line with our aim to evaluate the molecular alterations at acute tubular injury.

After sequencing, the AKI datasets were integrated with previously published healthy kidney datasets (Fig. 5A) (13). Following low-QC nuclei filtering and preprocessing, cell types in the snRNA-seq dataset were identified by cell type-specific marker gene expression (Fig. 5A and fig. S14A). For snATAC-seq, we performed label transfer with Seurat using this snRNA-seq dataset (18, 19). The snATAC-seq datasets were filtered using a 60% confidence threshold for cell type assignment. After the remaining preprocessing (see also Materials and Methods; fig. S15), integration of datasets with Harmony (20), and unsupervised clustering, we identified all the major cell types in snATAC-seq (Fig. 5A and fig. S14B). The QC metrics for both snRNA-seq and snATAC-seq datasets were variable compared to control (fig. S16), and those do not correlate with presumed causes of AKI and postmortem periods (data S12). This QC variability might potentially reflect numerous, complicated clinical and technical factors in AKI.

*VCAM1*+ PTCs (FR-PTCs) in healthy kidneys and *HAVCR1*+ injured PTCs in AKI kidneys were assigned to the same cluster after unsupervised clustering in both snRNA-seq and snATAC-seq (Fig. 5A), reflecting relative transcriptional and epigenetic similarities. We annotated this cluster as injury-related PTCs (iPTCs; Fig. 5A) containing both acutely injured PTCs of AKI kidneys and FR-PTCs of control kidneys. *VCAM1* expression was more abundant in iPTCs of control kidneys (FR-PTCs) compared to iPTCs of AKI (acutely injured PTCs; Fig. 5B and fig. S17A). We subset the injured PTCs to compare with the same number of FR-PTCs for the *VCAM1* expression level (fig. S18A), confirming that *VCAM1* was still highly expressed in FR-PTCs. The frequency of cells expressing *VCAM1* was also smaller in injured PTCs (~20%) compared to FR-PTCs (~30%) (fig. S18B). The *VCAM1* promoter was accessible among iPTCs in both healthy and AKI kidneys, although it was more prominent among iPTCs of healthy kidneys (FR-PTCs; fig. S17B), consistent with transcriptional data (figs. S17A and S18). Next, we evaluated the differential gene expression between injured PTCs in AKI and FR-PTCs in healthy kidneys (data S13 and S14). The most differentially expressed genes included *KCNIP4*, *AJAP1*, *SLC17A3* (up-regulated in injured PTCs), *DCC*, *FKBP5*, and *PDK4* (up-regulated in FR-PTCs) (Fig. 5B). *VCAM1* and *HAVCR1* were highly expressed in FR-PTCs in healthy kidneys and injured PTCs in AKI, respectively. (Fig. 5, B and C). In AKI, *HAVCR1* expression was also broadly up-regulated in the PTC cluster to a less extent compared to injured PTCs (Fig. 5C), suggesting mild injury or stress to all the segments in PTCs during ischemia. We also observed a higher expression of the NF- $\kappa$ B target genes (*CCL2*, *CSF1*, and *CD47*) in FR-PTCs in healthy kidneys (fig. S19A) compared to injured PTCs, consistent with mouse kidney data (Fig. 4). These findings suggested that the injured PTCs and FR-PTCs demonstrated a distinct gene expression signature, although they were clustered together in the integrated dataset. *CCL2* expression was highly specific to FR-PTCs in healthy kidneys, while its expression was rather up-regulated in parenchymal cells including endothelium, fibroblasts, and immune cells, in addition to distal nephron (distal convoluted tubules and principal cells) in AKI (fig. S19B). Similarly, *CSF1* expression was also up-regulated in parenchymal cells in AKI (fig. S19C). These findings indicate that the major source of these molecules may be different between healthy and AKI kidneys. *CD47* expression was the highest in FR-PTCs among PTC lineages,

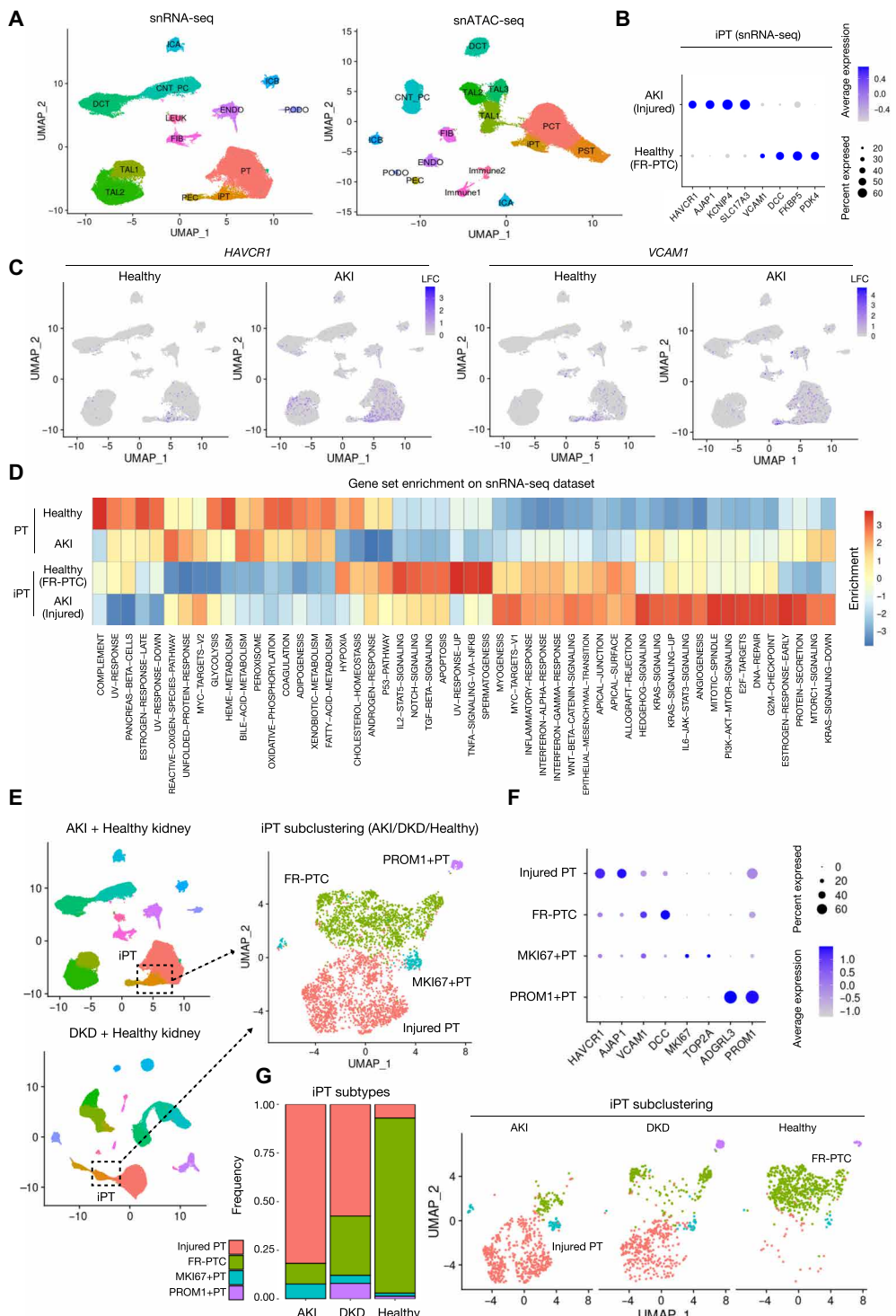


**Fig. 5. Heterogeneity of PTCs in the human kidneys with AKI.** (A) UMAP plot of snRNA-seq (left) or snATAC-seq (right) data for human kidneys with AKI ( $n = 4$ ) and controls ( $n = 5$ ). (B) Dot plot showing differential gene expressions in iPTCs between healthy (FR-PTCs) and AKI (injured PTCs). (C) UMAP plot showing gene expression levels of *HAVCR1* (left) or *VCAM1* (right), separately for healthy and AKI kidneys. The color scale represents a normalized LFC. (D) Heatmap showing the relative enrichment of hallmark gene sets among PTC lineages in snRNA-seq. (E) The iPTC cluster from the AKI dataset (top left) was merged with the iPTC (PT\_VCAM1) cluster from our previously published dataset for human DKD and healthy kidneys (bottom left). Following integration with Harmony, four subpopulations were identified on the UMAP (right). (F) Dot plot showing the marker gene expression among integrated iPTC subtypes. (G) UMAP plot of integrated iPTC subclustering separately shown for AKI, DKD, or healthy kidneys with the same number of cells (right). The frequencies of subtypes are also shown for each group (left). For dot plots, the diameter of the dot corresponds to the proportion of cells expressing the indicated gene and the density of the dot corresponds to average expression [(B) and (F)].

although *CD47* was broadly expressed in other cell types in both healthy and AKI kidneys (fig. S19D). This finding may be in line with the known role of *CD47* to avoid unnecessary phagocytosis (44) in healthy and AKI kidneys.

Gene set enrichment analysis (GSEA) (48) with hallmark gene sets using the Molecular Signatures Database (MsigDB) suggested differential activation of molecular pathways between acutely injured PTCs (iPTCs in AKI) and FR-PTCs (iPTCs in control kidney) (Fig. 5D). The gene set associated with TNF signaling via the NF- $\kappa$ B pathway was enriched in FR-PTCs, consistent with specific enrichment of the RELA binding motif in mouse FR-PTCs (Fig. 2C). In contrast, the gene set was related to proliferation such as G2-M checkpoint, Early region 2 binding factor (E2F) target, and DNA repair gene set, reflecting proliferation and regeneration of PTCs in injured PTCs.

We have previously performed single-cell multimodal analysis on diabetic kidney disease (DKD), elucidating heterogeneity of tubular epithelia in DKD. We found a greater proportion of *VCAM1*+ iPTCs in DKD samples compared to control samples (14). The DKD snRNA-seq dataset we have generated are from the samples with increased global glomerulosclerosis with interstitial fibrosis in histological evaluation (14), suggesting CKD. To interrogate the interrelationship between iPTCs of CKD and AKI, we integrated the iPTCs from our AKI datasets and those from DKD datasets. After subclustering, we identified four subtypes (Fig. 5E): injured PTCs (*HAVCR1* +), FR-PTCs (*VCAM1*+/*DCC* +), proliferating (*MKI67* +), and *PROM1*+PTCs (Fig. 5F). *PROM1*+PTCs were described as atypical PTCs expressing high *PROM1* in DKD, although their biological significance has remained elusive. In contrast, the proliferative PTCs were mainly derived from AKI samples (Fig. 5G). The healthy control datasets for AKI and those for DKD are from the same patients but generated by different chemistry (5' versus 3' v3 chemistry of the 10X Genomics platform). We confirmed that these healthy control datasets with different strategies merged well after integration with Harmony, validating our strategy (fig. S20). The iPTCs in DKD are a mixture of injured PTCs (~60%) and FR-PTCs (~30%) (Fig. 5G), indicating that iPTCs in DKD were composed of actively injured PTCs and accumulating FR-PTCs rather than a DKD-specific iPTC state. Collectively, these findings suggest a model of CKD progression whereby ongoing injury to PTCs drives their transition to an FR-PTC state.

TF motif enrichment analysis for PTCs in the snATAC-seq dataset (Fig. 6A and data S15 and S16) indicated *HNF4A* inactivation in both acutely injured PTCs and FR-PTCs (Fig. 6B). *JUN*::*FOS* and *NFE2L2* binding motifs were most enriched among acutely injured PTCs (Fig. 6C and fig. S5B). These findings were in agreement with the findings in mouse kidneys (Fig. 2D and fig. S5). *RELA* motif enrichment was observed among both acutely injured PTCs and FR-PTCs (Fig. 6D), although GSEA indicated that the NF- $\kappa$ B target genes were more abundantly expressed in FR-PTCs (Fig. 5D). We also observed transient enrichment of the *RELA* binding motif among acutely injured PTCs (day 2) following mouse IRI (Fig. 2E). Increased *RELA* binding motif availability in acutely injured PTCs may precede the activation of *RELA* and subsequent up-regulation of its target genes in FR-PTCs. Our multimodal single-nucleus analysis in human AKI kidneys is limited because each is a snapshot in time. Nevertheless, our analyses of both human and mouse PTCs collectively suggest that the PTC epigenetic alterations following AKI are largely conserved between humans and mice.

## CREB5 driving proliferative recovery of PTCs after IRI

Next, we asked if an interspecies approach might be useful to identify a novel molecular mechanism and potential therapeutic target in AKI. We recently developed regulatory network inference (RENIN), a regularized regression approach to predict gene regulatory networks using multimodal single-cell datasets (33). We applied RENIN to predict shared molecular mechanisms of PTC state regulation shared between mouse and human. Several TFs were predicted to drive maladaptive cell states in human kidneys. *NFAT5*, *GLIS3*, *KLF6*, and *CREB5* were identified as top-ranked accelerators of failed repair cell states in both mouse and human kidneys (Fig. 7A). These TFs were also top ranked as the TFs associated with injured cell states (Fig. 7A), suggesting that they are involved in both successful versus failed repair in acute PTC injury. *NFAT5* was previously described to be up-regulated following IRI (9) and predicted to promote failed repair in healthy human kidneys using RENIN (33). *KLF6* was found to be induced after IRI, contributing to kidney injury in mice and humans (49). *GLIS3* is broadly expressed in renal tubules and localized in primary cilia. *GLIS3* deficiency was shown to induce polycystic kidney disease in both humans and mice (50, 51), although it has no known role in AKI. Of note, *PAX8* was top ranked for promotion of both acute injury and failed repair in mouse PTCs (data S17 and S18). In contrast, *PAX8* was predicted to promote only the injured state but not the failed repair state in human PTCs (Fig. 7A and data S19 and S20), indicating potential differences in *PAX8* function during the AKI-to-CKD transition between human and mouse.

*CREB5*, a member of the CREB family, was recently found to be highly expressed in various types of cancers including colorectal (52), ovarian (53), hepatocellular (54), and prostate (55) and plays a promoting role in the development of cancers. Moreover, a recent line of evidence suggested the *CREB5* activation in PTCs in the kidneys of the patients with DKD (56). *CREB5* expression was also up-regulated broadly in PTCs in AKI (Fig. 7B and fig. S21, A and B), while its expression was localized in FR-PTCs in control kidneys (fig. S21, A and B). *CREB5* expression levels were further up-regulated in FR-PTCs in DKD (fig. S21C), suggesting that *CREB5* may play a more prominent role in FR-PTCs in CKD. In agreement with this finding, *CREB5* motif activity was broadly increased in PTCs in human AKI kidneys (Fig. 7C). In the mouse IRI dataset, *CREB5* binding motif accessibility was enriched in FR-PTCs and injured PTCs, especially in the S3 segment, which is the most vulnerable site in hypoxic injury (Fig. 7D). Up-regulation of *Creb5* expression was not clear in acutely injured mouse PTCs (fig. S21D), suggesting that enrichment of the *CREB5* binding motif in PTCs during the acute phase of IRI may reflect translocation of preexisting *CREB5* proteins to the nucleus from the cytoplasm rather than up-regulation of *CREB5* protein expression. In contrast, *Creb5* expression was prominently up-regulated in FR-PTCs in snRNA-seq (fig. S21D). To interrogate the role of *CREB5* in PTC recovery, we analyzed RNA-seq data of primary human PTCs targeted *CREB5* with siRNA knockdown. GSEA implicated up-regulation of the P53 pathway by *CREB5* knockdown, which may inhibit proliferation and induce cell cycle arrest (Fig. 7E). The primary human PTCs with *CREB5* knockdown had slower proliferation compared to control (Fig. 7F), suggesting that *CREB5* promotes cell proliferation and likely recovery in acutely injured PTC states. Deconvolution of bulk transcriptomic profile predicted that *CREB5* knockdown decreased the predicted frequency of injured PTCs (fig. S8D), in line with the

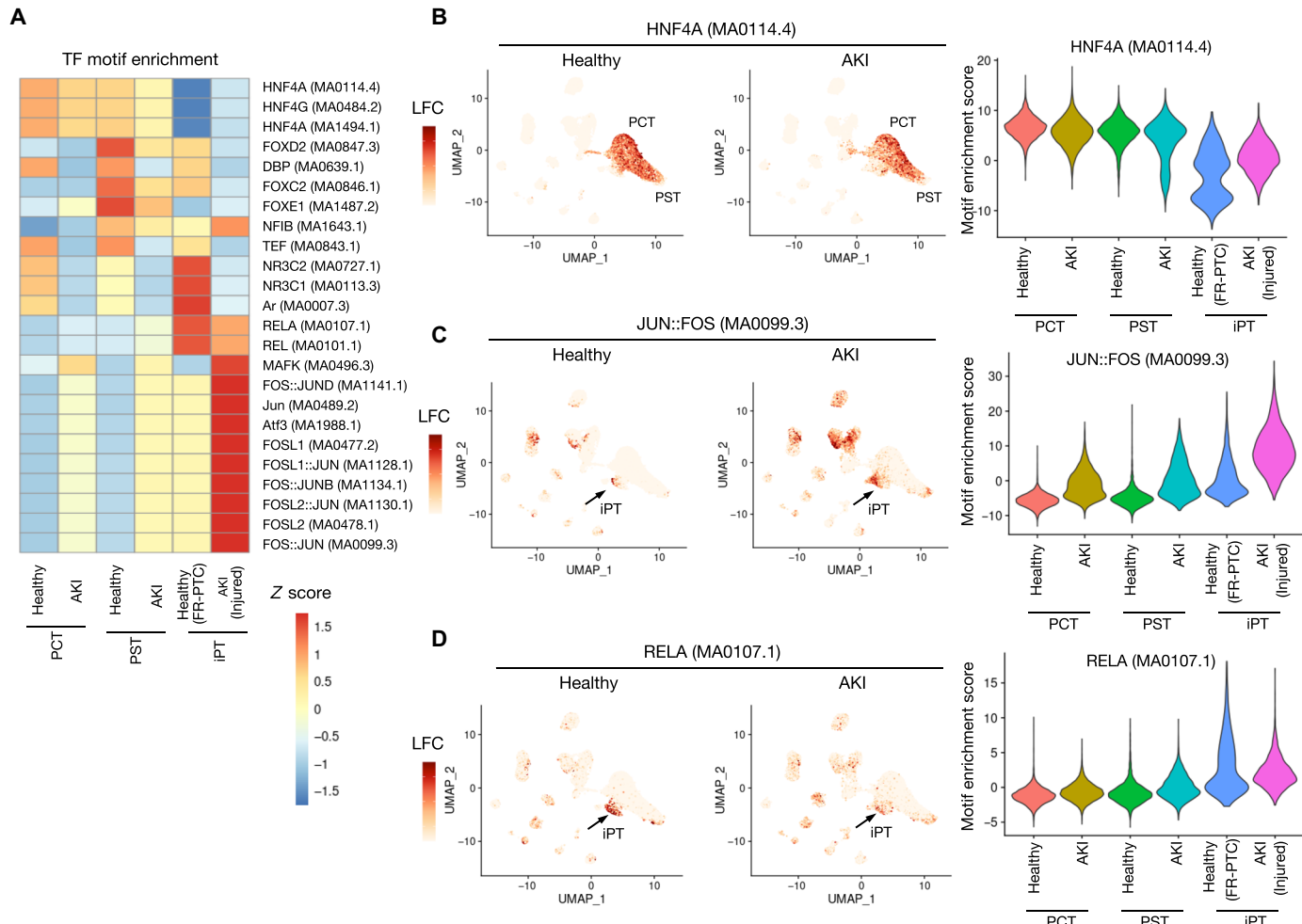


**Fig. 6. Single-nucleus chromatin accessibility profiling in human AKI.** (A) Heatmap showing the relative motif enrichment among PTC lineages in human snATAC-seq data. The most enriched motifs in each group are shown. (B to D) UMAP (left) and violin plot (right) displaying the relative motif enrichment (chromVAR score) among PTCs for HNF4A (MA0114.4 (B)), JUN::FOS (MA0099.3 (C)), or RELA (MA0107.1 (D)).

proposed role of CREB5 in proliferative PTC recovery (Fig. 7). This finding was consistent with down-regulation of proliferation marker *PCNA* and *FOXM1*, a master regulator of M phase progression, and its target *PLK1* by siRNA knockdown of *CREB5* in primary human PTCs (Fig. 7G). These findings collectively suggest that *CREB5* has a beneficial role in the recovery from acute injury by promoting proliferation, although persistent activation of *CREB5* in FR-PTCs may contribute to its unique gene expression signature (Fig. 7H). Together, these findings demonstrate the usefulness of interspecies multimodal approach to interrogate molecular mechanism of AKI and identify novel therapeutic targets.

## DISCUSSION

We generated and analyzed single-nucleus chromatin accessibility profiles across the spectrum of mouse acute injury and repair and compared to human AKI. Our integrative analysis of this atlas with our previously generated single-nucleus transcriptomic atlas from the same samples (8) allows us to understand the temporal dynamics of gene regulation during injury, repair, and failed repair. We

elucidated cell type-specific TF activities with an emphasis on the NF-κB effector *RELA* in injured and FR-PTC states along the time course. We mapped conserved *RELA* binding sites onto the mouse FR-PTC-specific accessible regions, revealing the cis-regulatory landscape driving failed repair defining genes. Furthermore, we generated paired snRNA-seq and snATAC-seq datasets from human AKI kidneys and compared with mouse IRI, shedding light on conserved and divergent gene regulatory networks between human and murine AKI.

Given that various renal insults drive an increase in *VCAM1*-expressing FR-PTCs along with infiltrating immune cells in both mouse and human kidneys (8, 10, 11, 13, 14), understanding the mechanism of emergence and maintenance of FR-PTCs and their biological roles will be critical to dissect the molecular mechanism driving AKI and the AKI-to-CKD transition. Here, we confirm and extend evidence implicating NF-κB activity as an important putative mediator of this cell state. A previous study in mice has shown that suppression of the NF-κB pathway reduced tubular apoptosis and chemokine-induced immune cell infiltration after IRI (57). Furthermore, phagocytosis of apoptotic cells by renal epithelial

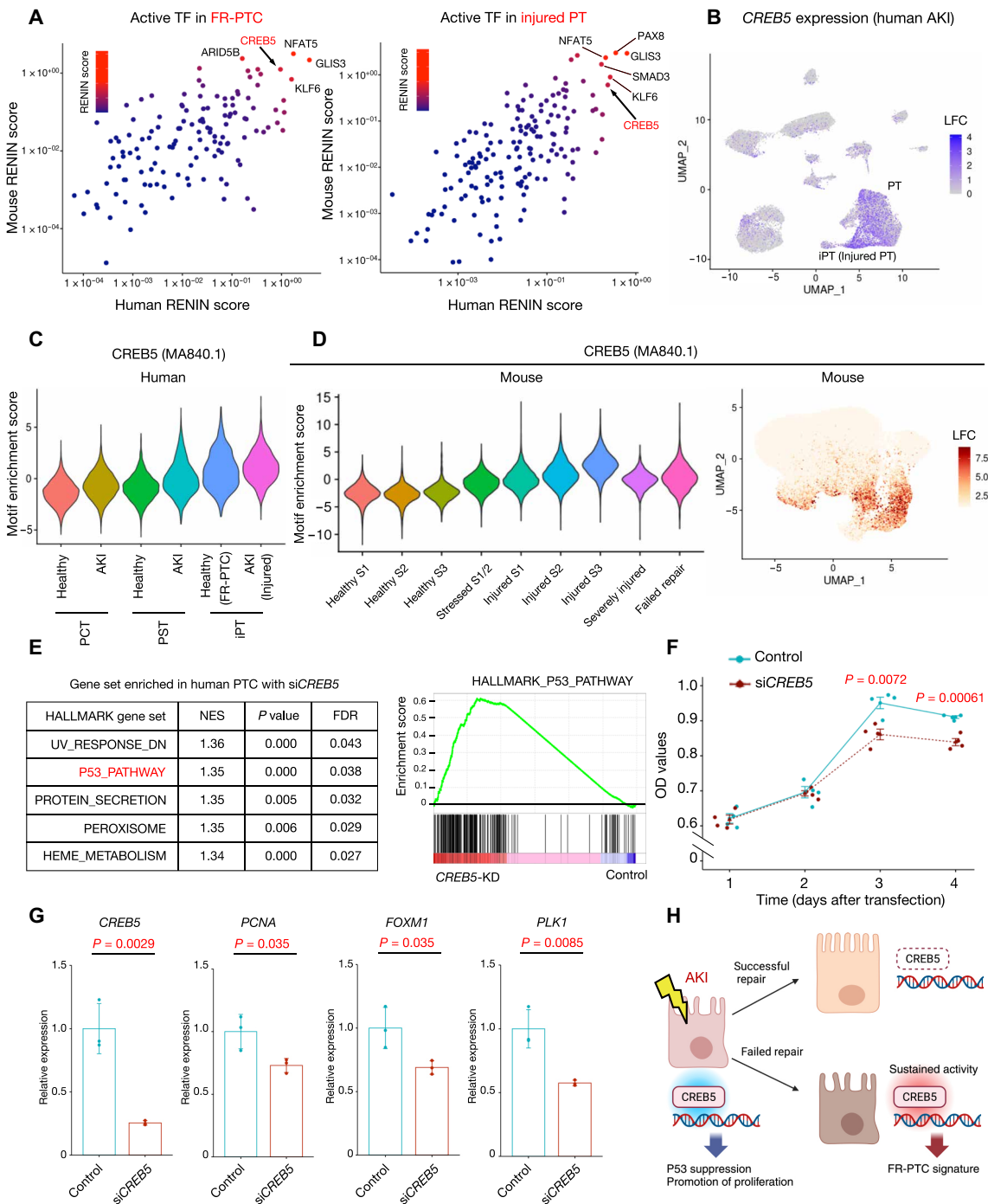


**Fig. 7. CREB5 driving the proliferative recovery of PTCs after IRI.** (A) RENIN regulatory scores to predict TF activities in the FR-PTC state (left) or injured PTC state (right) compared to normal PTCs in human (x axis) and mouse (y axis) multiomics datasets. A higher regulatory score indicates more activation. (B) UMAP plot showing the CREB5 expression level in human AKI. The color scale represents a normalized LFC. (C) Violin plot displaying the relative motif enrichment among PTC subtypes for CREB5 (MA0840.1) in the human snATAC-seq dataset. (D) Violin plot (left) and UMAP plot (right) displaying the relative motif enrichment for CREB5 (MA0840.1) among PTC subtypes in mouse kidneys. The color scale for the UMAP plot represents a normalized LFC. (E) GSEA with the hallmark gene sets on published bulk RNA-seq data of primary human PTCs with siRNA *CREB5* knockdown or control. The top-ranked gene sets with  $FDR < 0.05$  (left) and enrichment of P53 pathway genes in human primary PTCs with *CREB5* knockdown (right) are shown. NES, normalized enrichment score. (F) MTS assay in primary human PTCs showing decreased proliferation by *CREB5* knockdown compared with control. Each time point (1 to 4 days after siRNA transfection) consists of  $n = 4$  biological replicates. Student's *t* test for each time point. OD, optical density. (G) qPCR for *CREB5*, *PCNA*, *FOXM1*, and *PLK1* gene expression levels in primary PTCs with *CREB5* knockdown compared with control ( $n = 3$  biological replicates). Bar graphs represent the mean, and error bars are the SD. Student's *t* test. (H) Proposed role of *CREB5* in PTCs. Activation of *CREB5* in acute injury may promote PTC proliferation and recovery from the injury. Persistent up-regulation of *CREB5* in FR-PTCs may contribute to the FT-PTC gene expression signature. Schematic was created with BioRender.

cells mediated by HAVCR1 recruits p85 and inactivates NF- $\kappa$ B, suppressing the inflammatory pathway and protecting from IRI (58). These findings suggest that proximal tubular NF- $\kappa$ B activity may promote inflammation and exacerbate tubular injury during AKI. We confirmed enriched NF- $\kappa$ B motif availability among FR-PTCs in mouse kidneys with IRI (Fig. 2D), consistent with previous studies (8, 9, 11, 12). Furthermore, the NF- $\kappa$ B pathway was activated in injured PTCs as early as 2 days after injury before the FR-PTCs increased (Fig. 2E). We identified mouse FR-PTC DARs with conserved RELA binding sites identified by CUT&RUN on primary human PTCs (Fig. 3D). Given the previous line of evidence that TNF $\alpha$  alters the chromatin landscape to broadly reprogram the response to lipopolysaccharide in immune cells (59), TNF $\alpha$  treatment and NF- $\kappa$ B activation may alter the histone methylation and, subsequently, chromatin accessibility of PTCs around NF- $\kappa$ B binding sites, leading to transition to the failed repair cell state. The nearby genes of those DARs with conserved RELA binding sites were enriched with the genes for chemokines (Fig. 3E), which may allow FR-PTCs to interact with surrounding other cell types, including immune cells. For instance, we demonstrated the CCAN connecting the conserved NF- $\kappa$ B binding DAR and TSS of signaling molecules like *Ccl2*, *Csf1*, and *Cd47* as the potential modulators of the local immune cell landscape (Fig. 4 and figs. S9 to S13). Our findings highlight that NF- $\kappa$ B activation in FR-PTCs may have a role in shaping the local immune cell landscape during the AKI-to-CKD transition. Nevertheless, direct targeting of a TF is generally difficult. Alternative approaches may be to block its downstream targets or upstream stimulators. For example, anti-TNF $\alpha$  antibody has been applied in various autoimmune diseases. Several anti-inflammatory agents including aspirin, salicylate, and corticosteroids have been also proved to suppress NF- $\kappa$ B activation *in vivo* (60). We recently identified Traf2 and Nck interacting kinase (TNIK) as one of the exclusively up-regulated molecules in FR-PTCs. TNIK has been implicated in the NF- $\kappa$ B signaling pathway, and its depletion promotes inflammation and apoptosis (61). Although its mechanistic role in FR-PTCs has been elusive, modulating TNIK activity may represent a pro-repair therapeutic strategy potentially through modifying the NF- $\kappa$ B pathway. Thus, although direct targeting of RELA is difficult, there will be still opportunities to leverage our finding to develop a strategy to halt the AKI-to-CKD transition.

Injury-induced expression of proinflammatory mediators in PTCs includes CCL2, which was previously shown to promote inflammation and interstitial fibrosis after ischemic renal injury (36, 37). *Ccl2* expression was up-regulated in FR-PTCs likely in a RELA-dependent manner (Fig. 4). We identified myeloid lineage subsets including five macrophage subtypes as well as T cells and B cells after subclustering of immune cells in our dataset (figs. S11 to S13). Among them, *Plcb1*+Mac (Mac5) displayed the highest mRNA expression level (fig. S11C) and chromatin accessibility around the TSS of the *Ccr2* gene (fig. S12C), which encodes the CCL2 receptor. The number of the macrophages was increased and maintained at least until 6 weeks after IRI (fig. S12B). In contrast, *Itga9*+Mac (Mac2) subtype exists in the mouse kidneys without IRI (fig. S12B), suggesting that they are resident immune cells in the kidney. All the macrophage subtypes express *Csf1r* coding for the receptor for CSF1, which was also up-regulated in FR-PTCs (Fig. 4A). CSF1 may be also a stimulatory signal from PTCs to activate macrophages in IRI. FR-PTCs also express the gene encoding CD47 (fig. S9A), which protects cells from being phagocytosed by

immune cells and is often overexpressed in various cancers to avoid phagocytosis by tumor-associated macrophages (44). CD47 is a ligand for SIRP $\alpha$  on macrophages (fig. S11D), and binding CD47 to SIRP $\alpha$  initiates a molecular signaling to inhibit phagocytosis. Accumulated MRC1+ M2 macrophage initiates tissue fibrosis through TGFB1 expression, an irreversible hallmark of CKD (4). These findings suggest that the altered immune landscape by FR-PTCs contributes to the AKI-to-CKD transition.

To leverage our mouse dataset to identify a novel mechanism involved in the AKI-to-CKD transition, we also generated single-nucleus multimodal datasets for human AKI and intersected the gene regulatory networks between humans and mice. The gene regulatory network was constructed with RENIN, which we recently developed as a regularized regression approach (33) for multiomics datasets. Most of the TFs that were predicted to contribute to the injured state were also top ranked for promoting factors of the failed repair state, suggesting considerable overlap of the TFs being activated between acutely injured PTCs and FR-PTCs (Fig. 7A). Such TFs included CREB5, whose motif activity and mRNA expression were up-regulated in PTCs in human AKI (Fig. 7). CREB5 knockdown by siRNA in primary human PTCs up-regulated the genes associated with the P53 pathway, which may induce cell cycle arrest. Consistent with activation of the P53 pathway, CREB5 knockdown decreased proliferation of primary human PTCs (Fig. 7E), suggesting a pro-proliferation and pro-recovery role of CREB5 after PTC injury. We also found that CREB5 knockdown partly reduced the failed repair gene expression signature (33), implicating that sustained activation of CREB5 may also contribute to the failed repair state in the AKI-to-CKD transition.

In summary, we performed multimodal single-nucleus analysis of a mouse kidney IRI time course to define cell type-specific, temporally dynamic gene regulations. We also generated human AKI multiomics datasets to validate our mouse findings and leverage our mouse time-course dataset to understand the shared AKI mechanism and identify potential therapeutic targets. Our study is limited by the lack of spatial information of transcriptomic and epigenomic alteration. In the future, application of spatially resolved transcriptomics to the samples of kidneys with IRI will contribute to further dissection of intercellular communication in the AKI-to-CKD transition. Our single-nucleus multimodal analysis of mouse IRI kidneys provides a foundation on which to base future efforts to develop better diagnostic and therapeutic approaches for AKI.

## MATERIALS AND METHODS

### Experimental design

To comprehensively describe the cell-specific epigenomic perturbation in human and mouse AKI, we generated and sequenced snATAC-seq libraries from the frozen mouse kidney samples previously sequenced for snRNA-seq and previously published (8). Briefly, bilateral IRI on the kidney (18 min) was performed on male mice at 8 to 10 weeks of age, and control mice underwent sham surgery. Mice were euthanized with designated time points, and the kidneys were collected and frozen with liquid nitrogen. All mouse samples were harvested according to the animal experimental guidelines issued by the Animal Care and Use Committee protocol no. 20-0460 (Animal Welfare Assurance no. D16-00245) at Washington University in St. Louis. C57BL/6J mice were purchased from the Jackson Laboratory (Bar Harbor, ME).

Human AKI kidney cortical samples were obtained according to the protocol by the Washington University Institutional Review Board. Kidneys were discarded human donor kidneys from deceased patients (two male and two female, 55 to 69 years old; data S12). Samples were cut out from the outer cortex and frozen in liquid nitrogen. The single-cell dataset generated from control kidneys (10X Genomics Chromium Single Cell 3' v3 chemistry and 10X Genomics Chromium Single Cell ATAC v1) were already published (12).

### Nuclear dissociation for library preparation

For snATAC-seq, nuclei were isolated with Nuclei EZ Lysis buffer (NUC-101, Sigma-Aldrich) supplemented with protease inhibitor (5892791001, Roche). Samples were cut into <1 mm pieces, homogenized using a Dounce homogenizer (885302-0002, Kimble Chase) in 2 ml of ice-cold Nuclei EZ Lysis buffer, and incubated on ice for 5 min with an additional 2 ml of lysis buffer. The homogenate was filtered through a 40-μm cell strainer (43-50040-51, pluriSelect) and centrifuged at 500g for 5 min at 4°C. The pellet was resuspended, washed with 4 ml of buffer, and incubated on ice for 5 min. Following centrifugation, the pellet was resuspended in Nuclei Buffer (10X Genomics, PN-2000153), filtered through a 5-μm cell strainer (43-50005-03, pluriSelect), and counted. For snRNA-seq preparation, the RNase inhibitors (Promega, N2615 and Life Technologies, AM2696) were added to the lysis buffer, and the pellet was ultimately resuspended in nuclei suspension buffer [1x phosphate-buffered saline (PBS), 1% bovine serum albumin (BSA), and 0.1% ribonuclease (RNase) inhibitor]. All these processes were performed in a cold room at 4°C. Subsequently, 10X Chromium libraries were prepared according to the manufacturer's protocol.

### snATAC-seq for mouse kidneys and bioinformatics workflow

For mouse IRI kidneys, the snATAC-seq libraries were generated using 10X Genomics Chromium Single Cell ATAC v1 chemistry following nuclear dissociation. Libraries were sequenced on an Illumina NovaSeq instrument and counted with CellRanger ATAC v2.0 (10X Genomics) using mm10. The read configuration was 2x150-base pair (bp) paired-end reads. Sample index polymerase chain reaction (PCR) was performed at nine cycles. A mean of 457,383,804 reads were sequenced for each snATAC library ( $SD = 111,816,895$ ) with a median of 22,026 fragments per cell ( $SD = 15,328$ ). The data were aggregated with CellRanger ATAC v2.0, and the aggregated dataset (filtered\_peak\_bc\_matrix) was processed with Seurat v4.0.2 and its companion package Signac v1.4.0 (62). Low-quality cells were removed from the aggregated snATAC-seq library (subset the high-quality nuclei with peak region fragments > 2000, peak region fragments < 100000, %reads in peaks > 25, blacklist ratio < 0.08, nucleosome signal < 4, and TSS enrichment > 2). The barcodes representing doublets were determined with AMULET v1.1 (63) run on each snATAC-seq library, and those were filtered out from the integrated dataset (fig. S1A). A gene activity matrix was constructed by counting ATAC peaks within the gene body and 2 kbp upstream of the TSS using protein-coding genes annotated in the Ensembl database (19). FindTransferAnchors and TransferData functions were used for label transfer from the snRNA-seq dataset using gene activities, according to instructions (62). After label transfer, the snATAC-seq datasets were filtered using an 60% confidence threshold for low-resolution cell type assignment to remove low-quality nuclei and heterotypic doublets. Latent semantic indexing was

performed with term frequency inverse document frequency (TFIDF) followed by singular value decomposition (SVD). A k-nearest neighbors (KNN) graph was constructed to cluster cells with the Louvain algorithm. Batch effect was corrected with Harmony (20) using the RunHarmony function in Seurat. After clustering and cell type annotation based on lineage-specific gene activity (fig. S1, B to D), the nuclei with inconsistency between predicted low-resolution cell type and annotation based on lineage-specific gene activity were further filtered out to remove remaining doublets and low-quality nuclei (fig. S1, C and E). After filtering out these artifacts, the dataset was processed for batch effect correction with Harmony (20), clustering, and cell type annotation based on lineage-specific gene activity (fig. S2). The final snATAC-seq library contained a total of 193,731 peak regions among 157,000 nuclei. The number of fragments in peaks per nucleus was a mean of  $9292 \pm 6066$ , and %Fragments in peaks per nucleus was a mean of  $53.1 \pm 12.7\%$ . Fraction of reads in peaks, number of reads in peaks per cell, and ratio of reads in genomic blacklist regions per cell for each patient are shown in fig. S3. Differential chromatin accessibility among cell types was assessed with the Seurat FindMarkers function for peaks detected in at least 10% of cells with a likelihood ratio test and a log(fold change) threshold of 0.25 to identify differential chromatin accessibility. The nearby genes were determined by the ClosestFeature function. Bonferroni-adjusted P values were used to determine significance at an FDR of <0.05.

For subclustering of PTCs (PCTs and PSTs) or immune cells (Immune1 and Immune2) in snATAC-seq data, the target cell types were extracted from the integrated dataset (Fig. 1B). Following TFIDF/SVD and subclustering, the clusters with marker gene activities for other cell types were removed as remaining low-quality nuclei and doublets. Subsequently, TFIDF/SVD, processing with Harmony and subclustering, was performed with UMAP (Fig. 2 and fig. S12).

### snRNA-seq for human kidneys and bioinformatics workflow

For human AKI kidneys, snRNA-seq libraries were generated with 10X Genomics Chromium Single Cell 3' v3 chemistry following nuclear dissociation. A target of 10,000 nuclei were loaded onto each lane. The cDNA for snRNA libraries was amplified for 15 cycles. Libraries were sequenced on an Illumina NovaSeq instrument and counted with CellRanger v6.0.0 with --include-introns argument using GRCh38. The read configuration for the libraries was 2x150-bp paired-end reads. A mean of 503,452,820 reads ( $SD = 18,797,210$ ) were sequenced for each snRNA library corresponding to a mean of 54,336 reads per cell ( $SD = 26,822$ ). The mean sequencing saturation was  $38.8 \pm 8.0\%$ . The mean fraction of reads with a valid barcode (fraction of reads in cells) was  $39.6 \pm 15.4\%$ .

The output of CellRanger (filtered\_gene\_bc\_matrix) was processed through Seurat v4.0.2 (18). Ambient RNA contamination was corrected for each dataset by SoupX v1.5.0 (64) with automatically calculated contamination fraction. Each of the datasets was then processed to remove low-quality nuclei (nuclei with top 5% and bottom 1% in the distribution of feature count and RNA count and those with %Mitochondrial genes > 0.25). Heterotypic doublets were identified with DoubletFinder v2.0.3 (65), assuming 8% of barcodes represent heterotypic doublets, and resultant estimated doublets were removed after merging the datasets. The datasets were integrated in Seurat using the IntegrateData function with anchors identified by the FindIntegrationAnchors function. Subsequently,

the doublets and low-quality clusters were removed for these datasets. The major cell types were identified in the dataset for AKI kidneys (fig. S22). The control datasets ( $n = 5$ ) were previously published (GSE185948) (13). The AKI and control datasets were integrated with batch effect correction with Harmony v1.0 (20) using the RunHarmony function on assay RNA in Seurat. Then, there was a mean of  $8127 \pm 1692$  nuclei in control or  $8058 \pm 2971$  nuclei in AKI per the snRNA-seq library. The number of unique molecular identifiers per nucleus was a mean of  $3536 \pm 1914$  in control or  $3906 \pm 2429$  in AKI. The number of detected genes per nucleus was a mean of  $2222 \pm 803$  genes in control or  $2434 \pm 864$  genes in AKI. %Mitochondrial genes was  $0.027 \pm 0.050\%$  in control or  $0.028 \pm 0.048\%$  in AKI (fig. S16). Clustering was performed by constructing a KNN graph and applying the Louvain algorithm. Dimensional reduction was performed with UMAP, and individual clusters were annotated based on the expression of lineage-specific markers (fig. S14). Differential expressed genes among cell types were assessed with the Seurat FindMarkers function for transcripts detected in at least 10 or 20% (data S13) of cells using a log(fold change) threshold of 0.25. Bonferroni-adjusted  $P$  values were used to determine significance at an FDR of  $<0.05$ .

### snATAC-seq for human kidneys and bioinformatics workflow

For human AKI kidneys, snATAC-seq libraries were generated using 10X Genomics Chromium Single Cell ATAC v1 chemistry following nuclear dissociation. Libraries were sequenced on an Illumina NovaSeq instrument and counted with CellRanger ATAC v2.0 (10X Genomics) using GRCh38. The read configuration was 2x150-bp paired-end reads. Sample index PCR was performed at nine cycles. A mean of 402,063,865 reads were sequenced for each snATAC library ( $SD = 54,544,038$ ) with a median of 16,333 fragments per cell ( $SD = 2,033$ ). Five control snATAC-seq libraries (controls 1 to 5) were prepared and published in a prior study (GSE151302) (12). The libraries from control and AKI kidneys were aggregated with CellRanger ATAC v2.0. Subsequently, the aggregated dataset (filtered\_peak\_bc\_matrix) was processed with Seurat v4.0.2 and its companion package Signac v1.4.0 (62). Low-quality cells were removed from the aggregated snATAC-seq library (subset the high-quality nuclei with peak region fragments  $> 2500$ , peak region fragments  $< 25,000$ , %reads in peaks  $> 15$ , blacklist ratio  $< 0.1$ , nucleosome signal  $< 4$ , and TSS enrichment  $> 2$ ). A gene activity matrix was constructed by counting ATAC peaks within the gene body and 2 kbp upstream of the TSS using protein-coding genes (19) and used for label transfer with FindTransferAnchors and TransferData functions using the snRNA-seq dataset for the same human AKI samples, according to instructions (19). After label transfer, the snATAC-seq datasets were filtered using a 50% confidence threshold for low-resolution cell type assignment to remove low-quality cells and heterotypic doublets. A low-quality cluster with simultaneous marker gene activities with multiple cell types was further removed. Following TFIDF/SVD, batch effect was corrected with Harmony (20). After clustering and cell type annotation based on lineage-specific gene activity (fig. S15, A to D), the nuclei with inconsistency between predicted cell type and annotation based on lineage-specific gene activity were further filtered out to remove remaining doublets and low-quality nuclei (fig. S15E). The barcodes representing doublets determined with AMULET v1.1 (63) in each library were further filtered out from the integrated dataset (fig. S15A). After filtering out these artifacts, the dataset was

processed with Harmony (20) to remove batch effect. Clustering and cell type annotation were based on lineage-specific gene activity (fig. S14B). The final snATAC-seq library contained a total of 249,164 peak regions among 64,350 nuclei (31,397 nuclei for control and 32,953 nuclei for AKI) and represented all major cell types within the kidney cortex (Fig. 5A). The number of fragments in peaks per nucleus was a mean of  $8629 \pm 3575$  in control or  $8968 \pm 3526$  in AKI, and %Fragments in peaks per nucleus was a mean of  $59.4 \pm 10.7\%$  in control or  $56.7 \pm 12.8\%$  in AKI. Fraction of reads in peaks, number of reads in peaks per cell, and ratio of reads in genomic blacklist regions per cell for each patient are shown in fig. S16. Differential chromatin accessibility among cell types was assessed with the Seurat FindMarkers function for peaks detected in at least 10% of cells with a likelihood ratio test and a log(fold change) threshold of 0.25. The nearby genes were determined by the ClosestFeature function. Bonferroni-adjusted  $P$  values were used to determine significance at an FDR of  $<0.05$ .

### Integration of AKI and DKD snRNA-seq data

The iPTC cluster from the AKI dataset [ $n = 5$  control and  $n = 4$  AKI; generated with 3' v3 chemistry (10X Genomics)] and the PT\_VCAM1 (iPTC) cluster from the DKD dataset [ $n = 5$  control and  $n = 5$  DKD; generated with 5' chemistry (10X Genomics)] (14) were extracted. We excluded one control (control 6) from the DKD dataset due to increased sclerotic glomeruli (14). These datasets were integrated with Harmony (20) [RunHarmony function with group\_by.vars = "chemistry" (10X Genomics; 5' or 3' chemistry)]. Subsequently, clustering was performed by constructing a KNN graph and applying the Louvain algorithm. Dimensional reduction was performed with UMAP.

### Visualization of single-nucleus dataset features

Gene expressions (snRNA-seq) or gene activities (snATAC-seq) were visualized with the FeaturePlot (UMAP), VlnPlot (violin plot), or DotPlot (dot plot) function on Seurat. For feature plots of the genes with low expression levels (*CCL2*, *CSF1*, and *CD47*), cells were plotted in the order of expression (FeaturePlot function with order = T) (fig. S19). The fragment coverage around DARs in each cell type was visualized by the CoveragePlot function (Signac).

### Estimation of TF activity from snATAC-seq data

TF activity was estimated using the integrated snATAC-seq dataset and chromVAR v1.10.0 (22). The positional weight matrix was obtained from the JASPAR2022 database (collection = "CORE", tax\_group = "vertebrates", and all\_versions = F) (66). Cell type-specific chromVAR activities were calculated using the RunChromVAR wrapper in Signac v1.4.0. The chromVAR activity in each TF on the whole dataset was shown with the FeaturePlot function with max. cutoff = q99 and min.cutoff = q1 or the VlnPlot function.

### Construction of pseudotemporal trajectories

Cicero v1.3.5 (27) was used to generate pseudotemporal trajectories for the snATAC-seq dataset. First, the cell dataset (CDS) object was constructed from the peak count matrix in the Seurat object for PTC subtypes with the "make\_atac\_cds" function with binarize = F. Next, the CDS was preprocessed (num\_dim = 50), aligned to remove batch effect, and reduced onto a lower dimensional space with the "reduce\_dimension" function (reduction\_method = 'UMAP'; pre-process\_method = "Aligned") (67). After filtering potential doublets

and low-quality nuclei that express non-PTC type markers, the nuclei were clustered (cluster\_cells). Subsequently, cell ordering was performed with the learn\_graph function. The data were visualized with plot\_cells functions.

### Construction of the CCAN

Cicero v1.3.5 (27) was used to construct the CCAN for the snATAC-seq FR-PTCs (Fig. 4 and figs. S9 and S10) per instructions provided on GitHub ([https://cole-trapnell-lab.github.io/cicero-release/docs\\_m3/](https://cole-trapnell-lab.github.io/cicero-release/docs_m3/)). Briefly, the FR-PTC data were extracted from the integrated snATAC-seq dataset and converted to CDS objects using the make\_atac\_cds function. The CDS object was processed using the detect\_genes() and estimate\_size\_factors() functions with default parameters prior to dimensional reduction and conversion to a Cicero CDS object. The FR-PTC-specific CCAN was generated using the run\_cicero function with default parameters. The CCAN was visualized with plot\_connections function with coaccess\_cutoff = 0.2. CTCF binding sites (ChIP-seq peak track for 8-week-old male mouse kidney) generated and processed by ENCODE (45) were retrieved from the UCSC Genome Browser (35).

### Cell culture

Human primary PTCs (Lonza, CC-2553) were cultured with a renal epithelial cell growth medium kit (Lonza, CC-3190) in a humidified 5% CO<sub>2</sub> atmosphere at 37°C. Experiments were performed on early passages. Cells were plated at a density of  $1 \times 10^5$  cells per well in a 12-well plate, incubated overnight, and transfected with 40 pmol of siRNA for *RELA*, *RELB*, or *CREB5* [ON-TARGETplus SMARTpool siRNA (Horizon Discovery), L-003533-00, L-004767-00, and L-008436-00] or negative control siRNA [ON-TARGETplus Non-targeting Control Pool (Horizon Discovery), D-001810-10] using Lipofectamine RNAiMAX (Life Technologies) following the manufacturer's protocol. Cells were harvested at 72 hours after transfection for RNA isolation. For *RELA* or *RELB* knockdown, cells were also treated with or without TNFα (R&D Systems; 100 ng/ml) at 48 hours after transfection and harvested at 72 hours after transfection (24 hours after TNFα treatment).

### MTS assay

Primary human PTCs were seeded at  $2.5 \times 10^3$  cells per well on 96-well tissue culture plates 24 hours before transfection and transfected with 6 pmol of siRNA for *CREB5* [ON-TARGETplus SMARTpool siRNA (Horizon Discovery), L-008436-00] or negative control siRNA [ON-TARGETplus Non-targeting Control Pool (Horizon Discovery), D-001810-10] using Lipofectamine RNAiMAX (Life Technologies) following the manufacturer's protocol. Four replicates were prepared per group. Proliferation was measured using the CellTiter96 AQueous One Solution Cell Proliferation Assay (Promega, G3582) following the manufacturer's protocol. Optical density readings were obtained 2 hours following days 1, 2, 3, and 4.

### Quantitative PCR

Total RNA was extracted from primary human PTCs with the Direct-zol MicroPrep Kit (Zymo) following the manufacturer's instructions. The extracted RNA (2 µg) was reverse transcribed using the High-Capacity cDNA Reverse Transcription Kit (Life Technologies). Quantitative PCR (qPCR) was performed using the iTaq Universal SYBR Green Supermix (Bio-Rad). Data were normalized by the abundance of *GAPDH* mRNA. Primer sequences are shown in table S1.

### CUT&RUN assay

We performed the CUT&RUN assay with the CUTANA kit (EpiCypher, 14-1048) according to the manufacturer's instructions. The human RPTECs with early passages were seeded at  $8 \times 10^5$  cells on a 10-cm culture dish at the day before the assay and treated with or without TNFα (R&D Systems; 100 ng/ml) at 3 hours before the fixation. Formaldehyde (37%, Sigma-Aldrich, 25259) was directly added to the medium of the RPTECs to achieve a final concentration of 0.5% for 1 min in room temperature. Fixation reaction was quenched by adding glycine at a final concentration of 125 mM. The cells were treated with trypsin (Gibco, 0.05%) for 2 min at 37°C, scraped from a culture dish, and centrifuged at 500g for 5 min. The centrifugated cells were resuspended in PBS with 1% BSA and counted. A total of 500,000 cells in 100 µl of wash buffer were mixed and incubated with concanavalin A-conjugated paramagnetic beads. Antibodies were added to each sample [*RELA* antibody (Santa Cruz, sc-109, 1:25) or rabbit immunoglobulin G negative control antibody (EpiCypher, 13-0041, 1:50)]. The remaining steps were performed according to the manufacturer's instructions for cross-linked samples. Library preparation was performed using the NEBNext Ultra II DNA Library Prep Kit for Illumina (New England BioLabs, E7645S) with the manufacturer's instructions, including minor modifications indicated by the CUTANA kit. The libraries were sequenced on a NovaSeq instrument (Illumina, 150-bp paired-end reads). Fastq files were trimmed with Trim Galore [Cutadapt (v2.8)] and aligned with Bowtie2 (v2.3.5.1) (parameters: --local --very-sensitive-local --no-unal --no-mixed --no-discordant --phred33 -I 10 -X 700) using hg38. The Sequence Alignment/Map (SAM) files were converted to Binary Alignment Map (BAM) files with samtools (1.9). Peak calling was performed using MACS2 (v2.2.7.1) with default parameters. Visualization was performed with Integrated Genome Viewer (68) and bigWig files generated from BAM files using DeepTools (3.5.0). The visualization for modified histone (H3K4me3 and H3K27ac) in Fig. 3A was generated with previously published CUT&RUN data for human primary PTCs (33). CUT&RUN peaks were annotated with ChIPSeeker (v1.24.0) (69) using hg38. To convert the genome coordinates for human *RELA* binding sites (hg38) to those of the mouse genome (mm10), The Genome Browser Convert utility (<https://genome.ucsc.edu/cgi-bin/hgLiftOver>) was used with a minimum ratio of bases that must remap = 0.1 (35).

### Reanalysis of bulk RNA-seq

The bulk RNA-seq dataset for primary human PTCs with siRNA knockdown of *CREB5* or control was retrieved from GEO220222 (33). Briefly, the reads were then aligned with STAR v2.7.9a to the Ensembl release 101 primary assembly. Gene counts were calculated from the number of uniquely aligned, unambiguous reads by Subread:featureCount v2.0.3. The dataset was deconvoluted with snRNA-seq data for PTC subtypes of the IRI snRNA-seq dataset using CIBERSORTx executables v1.029 according to the instructions provided on the CIBERSORTx website (<https://cibersortx.stanford.edu>) (32). Before deconvolution, the genes in snRNA-seq data were converted to human annotations using biomaRt and ensembl. The PTC data [normal PTCs: PTS1/2/3, injured PTCs: New PT1, and FR-PTCs: New PT2 in our previous study (8)] were used for deconvolution. Briefly, cell type fraction (CIBERSORTx Fractions) was predicted with --single\_cell TRUE --rmbatchSmode TRUE --perm 100.

## GSEA and GO analysis

Single-nucleus GSEA was performed with the VISION v2.1.0 R package according to the instructions provided on GitHub (<https://github.com/YosefLab/VISION>) (48), using Hallmark gene sets obtained from the MsigDB v7.4 distributed at the GSEA website. The heatmaps were generated with pheatmap v1.0.12 from gene set enrichment scores averaged in each cell type (Fig. 6C). The bulk RNA-seq data were analyzed with GSEA v4.0.3 software (Broad Institute) (70) with Hallmark gene sets. The top-ranked gene set list in Fig. 7E only displays those with FDR < 0.05. The whole list including FDR = 0.05 or more is available in data S21. GO term analysis was performed with Gene Ontology Resource (<https://geneontology.org/>) (71, 72).

## Gene regulatory network analysis with RENIN

To construct gene regulatory networks, we first generated CCANs in our snATAC-seq datasets with Cicero v1.3.9 (27). Within each CCAN, we identified peaks that overlapped with the 2-kilo-bp (kbp) promoter region or gene body for genes that were differentially expressed between the PTC and iPTC clusters in each of the control and AKI group in the human snRNA-seq dataset or between the healthy PTCs (PTS1–3) and acutely injured PTCs (New PT1) or FR-PTCs (New PT2) clusters in the mouse snRNA-seq dataset (8). Differentially expressed genes with linked CCANs were included for TF modeling. For each species, we then used the filtered cisBP v0.2 motif database provided by the chromVARmotifs package and JASPAR2022 to identify predicted TF binding sites within each differentially expressed gene-linked CCAN. A preliminary list of TFs that regulate each differentially expressed gene was generated by aggregating TFs with at least one predicted binding motif within each gene's CCAN. From the preliminary list of TFs regulating each differentially expressed gene, we then used the adaptive elastic net-based RENIN to generate parametric gene regulatory networks for each gene. We then ranked TFs by the sum of their coefficients across differentially expressed genes between groups, multiplied by each TF's mean proximal tubular expression. Regulatory coefficients for differentially expressed genes that were up-regulated in the normal PTC cluster versus the injury-associated cluster were multiplied by -1 to allow for identification of failed repair or injury association for each TF. To evaluate interspecies RENIN scores (Fig. 7A), the mouse genes were converted to human genes using biomaRt and ensembl with the getLDS function.

## Statistical analysis

No statistical methods were used to predetermine the sample size for single-nucleus analysis. Experiments were not randomized, and investigators were not blinded to allocation during library preparation, experiments, or analysis. Bonferroni-adjusted *P* values were used to determine significance for differential gene expression or accessibility. The qPCR data (Figs. 4 and 7 and fig. S9) and bulk RNA-seq deconvolution data (fig. S8, C and D) are presented as means  $\pm$  SD and were compared between groups with two-sided Student's *t* test (Fig. 7) or one-way analysis of variance (ANOVA) with post hoc Tukey test (Fig. 4 and figs. S8 and S9). The MTS assay data were compared between groups with two-sided Student's *t* test at each time point (Fig. 7). A *P* value of <0.05 was considered statistically significant.

## Supplementary Materials

This PDF file includes:

Figs. S1 to S22

## Table S1

Legends for data S1 to S21

## Other Supplementary Material for this manuscript includes the following:

Data S1 to S21

## REFERENCES AND NOTES

- A. S. Levey, M. T. James, Acute kidney injury. *Ann. Intern. Med.* **167**, ITC66–ITC80 (2017).
- C. Ronco, R. Bellomo, J. A. Kellum, Acute kidney injury. *Lancet* **394**, 1949–1964 (2019).
- L. S. Chawla, P. W. Eggers, R. A. Star, P. L. Kimmel, Acute kidney injury and chronic kidney disease as interconnected syndromes. *N. Engl. J. Med.* **371**, 58–66 (2014).
- T. Chen, Q. Cao, Y. Wang, D. C. H. Harris, M2 macrophages in kidney disease: Biology, therapies, and perspectives. *Kidney Int.* **95**, 760–773 (2019).
- H. I. Han, L. B. Skvarca, E. B. Espiritu, A. J. Davidson, N. A. Hukriede, The role of macrophages during acute kidney injury: Destruction and repair. *Pediatr. Nephrol.* **34**, 561–569 (2019).
- B. D. Humphreys, Mechanisms of renal fibrosis. *Annu. Rev. Physiol.* **80**, 309–326 (2018).
- E. R. Gibney, C. M. Nolan, Epigenetics and gene expression. *Heredity* **105**, 4–13 (2010).
- Y. Kiritu, H. Wu, K. Uchimura, P. C. Wilson, B. D. Humphreys, Cell profiling of mouse acute kidney injury reveals conserved cellular responses to injury. *Proc. Natl. Acad. Sci. U.S.A.* **117**, 15874–15883 (2020).
- L. M. S. Gerhardt, J. Liu, K. Koppitch, P. E. Cippà, A. P. McMahon, Single-nuclear transcriptomics reveals diversity of proximal tubule cell states in a dynamic response to acute kidney injury. *Proc. Natl. Acad. Sci. U.S.A.* **118**, e2026684118 (2021).
- S. Ide, Y. Kobayashi, K. Ide, S. A. Strausser, K. Abe, S. Herbek, L. L. O'Brien, S. D. Crowley, L. Barisoni, A. Tata, P. R. Tata, T. Souria, Ferroptotic stress promotes the accumulation of pro-inflammatory proximal tubular cells in maladaptive renal repair. *eLife* **10**, e68603 (2021).
- L. M. S. Gerhardt, K. Koppitch, J. van Gestel, J. Guo, S. Cho, H. Wu, Y. Kiritu, B. D. Humphreys, A. P. McMahon, Lineage tracing and single-nucleus multiomics reveal novel features of adaptive and maladaptive repair after acute kidney injury. *J. Am. Soc. Nephrol.* **34**, 554–571 (2023).
- Y. Muto, P. C. Wilson, N. Ledru, H. Wu, H. Dimke, S. S. Waikar, B. D. Humphreys, Single cell transcriptional and chromatin accessibility profiling redefine cellular heterogeneity in the adult human kidney. *Nat. Commun.* **12**, 2190 (2021).
- Y. Muto, E. E. Dixon, Y. Yoshimura, H. Wu, K. Omachi, N. Ledru, P. C. Wilson, A. J. King, N. Eric Olson, M. G. Gunawan, J. J. Kuo, J. H. Cox, J. H. Miner, S. L. Seliger, O. M. Woodward, P. A. Welling, T. J. Watnick, B. D. Humphreys, Defining cellular complexity in human autosomal dominant polycystic kidney disease by multimodal single cell analysis. *Nat. Commun.* **13**, 6497 (2022).
- P. C. Wilson, Y. Muto, H. Wu, A. Karihaloo, S. S. Waikar, B. D. Humphreys, Multimodal single cell sequencing implicates chromatin accessibility and genetic background in diabetic kidney disease progression. *Nat. Commun.* **13**, 5253 (2022).
- Y.-H. Chou, S.-Y. Pan, Y.-H. Shao, H.-M. Shih, S.-Y. Wei, C.-F. Lai, W.-C. Chiang, C. Schrimpf, K.-C. Yang, L.-C. Lai, Y.-M. Chen, T.-S. Chu, S.-L. Lin, Methylation in pericytes after acute injury promotes chronic kidney disease. *J. Clin. Invest.* **130**, 4845–4857 (2020).
- M. Nangaku, Y. Hirakawa, I. Mimura, R. Inagi, T. Tanaka, Epigenetic changes in the acute kidney injury-to-chronic kidney disease transition. *Nephron* **137**, 256–259 (2017).
- X. Cao, J. Wang, T. Zhang, Z. Liu, L. Liu, Y. Chen, Z. Li, Y. Zhao, Q. Yu, T. Liu, J. Nie, Y. Niu, Y. Chen, L. Yang, L. Zhang, Chromatin accessibility dynamics dictate renal tubular epithelial cell response to injury. *Nat. Commun.* **13**, 7322 (2022).
- Y. Hao, S. Hao, E. Andersen-Nissen, W. M. Mauck, S. Zheng, A. Butler, M. J. Lee, A. J. Wilk, C. Darby, M. Zager, P. Hoffman, M. Stoeckius, E. Papalexi, E. P. Mimitou, J. Jain, A. Srivastava, T. Stuart, L. M. Fleming, B. Yeung, A. J. Rogers, J. M. McElrath, C. A. Blish, R. Gottardo, P. Smibert, R. Satija, Integrated analysis of multimodal single-cell data. *Cell* **184**, 3573–3587.e29 (2021).
- T. Stuart, A. Srivastava, S. Madad, C. A. Lareau, R. Satija, Single-cell chromatin state analysis with Signac. *Nat. Methods* **18**, 1333–1341 (2021).
- I. Korsunsky, N. Millard, J. Fan, K. Slowikowski, F. Zhang, K. Wei, Y. Baglaenko, M. Brenner, P. Loh, S. Raychaudhuri, Fast, sensitive and accurate integration of single-cell data with Harmony. *Nat. Methods* **16**, 1289–1296 (2019).
- J. Liu, S. Kumar, E. Dolzhenko, G. F. Alvarado, J. Guo, C. Lu, Y. Chen, M. Li, M. C. Dessing, R. K. Parvez, P. E. Cippà, A. M. Krautberger, G. Saribekyan, A. D. Smith, A. P. McMahon, Molecular characterization of the transition from acute to chronic kidney injury following ischemia/reperfusion. *JCI Insight* **2**, e94716 (2017).
- A. N. Schep, B. Wu, J. D. Buenrostro, W. J. Greenleaf, chromVAR: Inferring transcription-factor-associated accessibility from single-cell epigenomic data. *Nat. Methods* **14**, 975–978 (2017).
- L. M. Shelton, B. K. Park, I. M. Copple, Role of Nrf2 in protection against acute kidney injury. *Kidney Int.* **84**, 1090–1095 (2013).
- M. Yamamoto, T. W. Kensi, H. Motohashi, The KEAP1-NRF2 system: A thiol-based sensor-effector apparatus for maintaining redox homeostasis. *Physiol. Rev.* **98**, 1169–1203 (2018).

25. J. V. Bonventre, L. Yang, Cellular pathophysiology of ischemic acute kidney injury. *J. Clin. Invest.* **121**, 4210–4221 (2011).
26. C.-T. Ong, V. G. Corces, CTCF: An architectural protein bridging genome topology and function. *Nat. Rev. Genet.* **15**, 234–246 (2014).
27. H. A. Pliner, J. S. Packer, J. L. McFaline-Figueroa, D. A. Cusanovich, R. M. Daza, D. Aghamirzaie, S. Srivatsan, X. Qiu, D. Jackson, A. Minkina, A. C. Adey, F. J. Steemers, J. Shendure, C. Trapnell, Cicero predicts *cis*-regulatory DNA interactions from single-cell chromatin accessibility data. *Mol. Cell* **71**, 858–871.e8 (2018).
28. M. Bleu, S. Gaulis, R. Lopes, K. Sprouffske, V. Apfel, S. Holwerda, M. Pregnolato, U. Yildiz, V. Cordero, A. F. M. Dost, J. Knehr, W. Carbone, F. Lohmann, C. Y. Lin, J. E. Bradner, A. Kauffmann, L. Tordella, G. Roma, G. G. Galli, PAX8 activates metabolic genes via enhancer elements in Renal Cell Carcinoma. *Nat. Commun.* **10**, 3739 (2019).
29. S. A. Patel, S. Hirosue, P. Rodrigues, E. Vojtasova, E. K. Richardson, J. Ge, S. E. Syarfruddin, A. Speed, E. K. Papachristou, D. Baker, D. Clarke, S. Purvis, L. Wesolowski, A. Dyas, L. Castillon, V. Caraffini, D. Bihary, C. Yong, D. J. Harrison, G. D. Stewart, M. J. Machiela, M. P. Purdue, S. J. Chanock, A. Y. Warren, S. A. Samarajiwa, J. S. Carroll, S. Vanharanta, The renal lineage factor PAX8 controls oncogenic signalling in kidney cancer. *Nature* **606**, 999–1006 (2022).
30. A. J. Peired, G. Antonelli, M. L. Angelotti, M. Allinovi, F. Guzzi, A. Sisti, R. Semeraro, C. Conte, B. Mazzinghi, S. Nardi, M. E. Melica, L. De Chiara, E. Lazzari, L. Lasagni, T. Lottini, S. Landini, S. Giglio, A. Mari, F. Di Maida, A. Antonelli, F. Porziglia, R. Schiavina, V. Ficarra, D. Facchiano, M. Gacci, S. Serni, M. Carini, G. Netto, R. M. Roberto, A. Magi, C. F. Christiansen, M. Rotondi, H. Liapis, H.-J. Anders, A. Minervini, M. R. Raspollini, P. Romagnani, Acute kidney injury promotes development of papillary renal cell adenoma and carcinoma from renal progenitor cells. *Sci. Transl. Med.* **12**, eaaw6003 (2020).
31. P. J. Skene, S. Henikoff, An efficient targeted nuclease strategy for high-resolution mapping of DNA binding sites. *eLife* **6**, e21856 (2017).
32. A. M. Newman, C. B. Steen, C. L. Liu, A. J. Gentles, A. A. Chaudhuri, F. Scherer, M. S. Khodadoust, M. S. Esfahani, B. A. Luca, D. Steiner, M. Diehn, A. A. Alizadeh, Determining cell type abundance and expression from bulk tissues with digital cytometry. *Nat. Biotechnol.* **37**, 773–782 (2019).
33. N. Ledru, P. C. Wilson, Y. Muto, Y. Yoshimura, H. Wu, D. Li, A. Asthana, S. G. Tullius, S. S. Waikar, G. Orlando, B. D. Humphreys, Predicting proximal tubule failed repair drivers through regularized regression analysis of single cell multiomic sequencing. *Nat. Commun.* **15**, 1291 (2024).
34. M. S. Hayden, S. Ghosh, Regulation of NF- $\kappa$ B by TNF family cytokines. *Semin. Immunol.* **26**, 253–266 (2014).
35. W. J. Kent, C. W. Sugnet, T. S. Furey, K. M. Roskin, T. H. Pringle, A. M. Zahler, D. Haussler, The human genome browser at UCSC. *Genome Res.* **12**, 996–1006 (2002).
36. L. Xu, D. Sharkey, L. G. Cantley, Tubular GM-CSF promotes late MCP-1/CCR2-mediated fibrosis and inflammation after ischemia/reperfusion injury. *J. Am. Soc. Nephrol.* **30**, 1825–1840 (2019).
37. L. Li, L. Huang, S.-S. J. Sung, A. L. Vergis, D. L. Rosin, C. E. Rose, P. I. Lobo, M. D. Okusa, The chemokine receptors CCR2 and CX3CR1 mediate monocyte/macrophage trafficking in kidney ischemia-reperfusion injury. *Kidney Int.* **74**, 1526–1537 (2008).
38. I. Ushach, A. Zlotnik, Biological role of granulocyte macrophage colony-stimulating factor (GM-CSF) and macrophage colony-stimulating factor (M-CSF) on cells of the myeloid lineage. *J. Leukoc. Biol.* **100**, 481–489 (2016).
39. M.-Z. Zhang, B. Yao, S. Yang, L. Jiang, S. Wang, X. Fan, H. Yin, K. Wong, T. Miyazawa, J. Chen, I. Chang, A. Singh, R. C. Harris, CSF-1 signaling mediates recovery from acute kidney injury. *J. Clin. Invest.* **122**, 4519–4532 (2012).
40. Y. Wang, J. Chang, B. Yao, A. Niu, E. Kelly, M. C. Breeggemann, S. L. Abboud Werner, R. C. Harris, M.-Z. Zhang, Proximal tubule-derived colony stimulating factor-1 mediates polarization of renal macrophages and dendritic cells, and recovery in acute kidney injury. *Kidney Int.* **88**, 1274–1282 (2015).
41. J. Menke, Y. Iwata, W. A. Rabacal, R. Basu, Y. G. Yeung, B. D. Humphreys, T. Wada, A. Schwarting, E. R. Stanley, V. R. Kelley, CSF-1 signals directly to renal tubular epithelial cells to mediate repair in mice. *J. Clin. Invest.* **119**, 2330–2342 (2009).
42. L. Meziani, M. Mondini, B. Petit, A. Boissonnas, V. Thomas de Montpreville, O. Mercier, M.-C. Vozenin, E. Deutsch, CSF1R inhibition prevents radiation pulmonary fibrosis by depletion of interstitial macrophages. *Eur. Respir. J.* **51**, 1702120 (2018).
43. N. Joshi, S. Watanabe, R. Verma, R. P. Jablonski, C.-I. Chen, P. Cheresh, N. S. Markov, P. A. Reyfman, A. C. McQuattie-Pimentel, L. Sichizya, Z. Lu, R. Piseaux-Aillon, D. Kirchenbuechler, A. S. Flozak, C. J. Gottardi, C. M. Cuda, H. Perlman, M. Jain, D. W. Kamp, G. R. S. Budinger, A. V. Misharin, A spatially restricted fibrotic niche in pulmonary fibrosis is sustained by M-CSF/M-CSFR signalling in monocyte-derived alveolar macrophages. *Eur. Respir. J.* **55**, 1900646 (2020).
44. S. Jaiswal, M. P. Chao, R. Majeti, I. L. Weissman, Macrophages as mediators of tumor immunosurveillance. *Trends Immunol.* **31**, 212–219 (2010).
45. ENCODE Project Consortium, J. E. Moore, M. J. Purcaro, H. E. Pratt, C. B. Epstein, N. Shores, J. Adrian, T. Kawli, C. A. Davis, A. Dobin, R. Kaul, J. Halow, E. L. Van Nostrand, P. Freese, D. U. Gorkin, Y. Shen, Y. He, M. Mackiewicz, F. Pauli-Behn, B. A. Williams, A. Mortazavi, C. A. Keller, X.-O. Zhang, S. I. Elhajjajy, J. Huey, D. E. Dickel, V. Snetkova, X. Wei, X. Wang, J. C. Rivera-Mulia, J. Rozowsky, J. Zhang, S. B. Chhetri, J. Zhang, A. Victorsen, K. P. White, A. Visel, G. W. Yeo, C. B. Burge, E. Lécuyer, D. M. Gilbert, J. Dekker, J. Rinn, E. M. Mendenhall, J. R. Ecker, M. Kellis, R. J. Klein, W. S. Noble, A. Kundaje, R. Guigó, P. J. Farnham, J. M. Cherry, R. M. Myers, B. Ren, B. R. Graveley, M. B. Gerstein, L. A. Pennacchio, M. P. Snyder, B. E. Bernstein, B. Wold, R. C. Hardison, T. R. Gingeras, J. A. Stamatoyannopoulos, Z. Weng, Expanded encyclopaedias of DNA elements in the human and mouse genomes. *Nature* **583**, 699–710 (2020).
46. J. Barrera-Chimal, G. R. Estrela, S. M. Lechner, S. Giraud, S. El Moghrabi, S. Kaaki, P. Kolkhof, T. Huet, F. Jaisser, The myeloid mineralocorticoid receptor controls inflammatory and fibrotic responses after renal injury via macrophage interleukin-4 receptor signaling. *Kidney Int.* **93**, 1344–1355 (2018).
47. J. M. Luther, A. B. Fogo, The role of mineralocorticoid receptor activation in kidney inflammation and fibrosis. *Kidney Int. Suppl.* **12**, 63–68 (2022).
48. D. DeTomaso, M. G. Jones, M. Subramanian, T. Ashuach, C. J. Ye, N. Yosef, Functional interpretation of single cell similarity maps. *Nat. Commun.* **10**, 4376 (2019).
49. S. E. Piret, Y. Guo, A. A. Attallah, S. J. Horne, A. Zollman, D. Owusu, J. Henein, V. S. Sidorenko, M. P. Revelo, T. Hato, A. Ma'ayan, J. C. He, S. K. Mallipattu, Krüppel-like factor 6-mediated loss of BCAA catabolism contributes to kidney injury in mice and humans. *Proc. Natl. Acad. Sci. U.S.A.* **118**, e2024414118 (2021).
50. H. S. Kang, J. Y. Beak, Y.-S. Kim, R. Herbert, A. M. Jetten, Glis3 is associated with primary cilia and Wwt1/TAZ and implicated in polycystic kidney disease. *Mol. Cell. Biol.* **29**, 2556–2569 (2009).
51. V. Senéci, C. Chelala, S. Duchatelet, D. Feng, H. Blanc, J.-C. Cossec, C. Charon, M. Nicolino, P. Boileau, D. R. Cavener, P. Bougnères, D. Taha, C. Julier, Mutations in GLIS3 are responsible for a rare syndrome with neonatal diabetes mellitus and congenital hypothyroidism. *Nat. Genet.* **38**, 682–687 (2006).
52. S. Wang, J. Qiu, L. Liu, C. Su, L. Qi, C. Huang, X. Chen, Y. Zhang, Y. Ye, Y. Ding, L. Liang, W. Liao, CREB5 promotes invasiveness and metastasis in colorectal cancer by directly activating MET. *J. Exp. Clin. Cancer Res.* **39**, 168 (2020).
53. S. He, Y. Deng, Y. Liao, X. Li, J. Liu, S. Yao, CREB5 promotes tumor cell invasion and correlates with poor prognosis in epithelial ovarian cancer. *Oncol. Lett.* **14**, 8156–8161 (2017).
54. J. Wu, S.-T. Wang, Z.-J. Zhang, Q. Zhou, B.-G. Peng, CREB5 promotes cell proliferation and correlates with poor prognosis in hepatocellular carcinoma. *Int. J. Clin. Exp. Pathol.* **11**, 4908–4916 (2018).
55. J. H. Hwang, J.-H. Seo, M. L. Beshiri, S. Wankowicz, D. Liu, A. Cheung, J. Li, X. Qiu, A. L. Hong, G. Botta, L. Golumb, C. Richter, J. So, G. J. Sandoval, A. O. Giacomelli, S. H. Ly, C. Han, C. Dai, H. Pakula, A. Sheahan, F. Piccioni, O. Gjoerup, M. Loda, A. G. Sowalsky, L. Ellis, H. Long, D. E. Root, K. Kelly, E. M. Van Allen, M. L. Freedman, A. D. Choudhury, W. C. Hahn, CREB5 promotes resistance to androgen-receptor antagonists and androgen deprivation in prostate cancer. *Cell Rep.* **29**, 2355–2370.e6 (2019).
56. W. Shi, W. Le, Q. Tang, S. Shi, J. Shi, Regulon analysis identifies protective FXR and CREB5 in proximal tubules in early diabetic kidney disease. *BMC Nephrol.* **24**, 180 (2023).
57. L. Markó, E. Vigolo, C. Hinze, J.-K. Park, G. Roél, A. Balogh, M. Choi, A. Wübken, J. Cording, I. E. Blasig, F. C. Luft, C. Scheidereit, K. M. Schmidt-Ott, R. Schmidt-Ullrich, D. N. Müller, Tubular epithelial NF- $\kappa$ B activity regulates ischemic AKI. *J. Am. Soc. Nephrol.* **27**, 2658–2669 (2016).
58. L. Yang, C. R. Brooks, S. Xiao, V. Sabbisetti, M. Y. Yeung, L.-L. Hsiao, T. Ichimura, V. Kuchroo, J. V. Bonventre, KIM-1-mediated phagocytosis reduces acute injury to the kidney. *J. Clin. Invest.* **125**, 1620–1636 (2015).
59. S. H. Park, K. Kang, E. Giannopoulou, Y. Qiao, K. Kang, G. Kim, K.-H. Park-Min, L. B. Ivashkiv, Type I interferons and the cytokine TNF cooperatively reprogram the macrophage epigenome to promote inflammatory activation. *Nat. Immunol.* **18**, 1104–1116 (2017).
60. H. Yu, L. Lin, Z. Zhang, H. Zhang, H. Hu, Targeting NF- $\kappa$ B pathway for the therapy of diseases: Mechanism and clinical study. *Signal Transduct. Target. Ther.* **5**, 209 (2020).
61. S. T. J. Bradford, H. Wu, Y. Kirita, C. Chen, N. P. Malvin, Y. Yoshimura, Y. Muto, B. D. Humphreys, TNK depletion induces inflammation and apoptosis in injured renal proximal tubule epithelial cells. *Am. J. Physiol. Renal Physiol.* **326**, F827–F838 (2024).
62. T. Stuart, A. Srivastava, S. Madad, C. A. Lareau, R. Satija, Single-cell chromatin state analysis with Signac. *Nat. Methods* **18**, 1333–1341 (2021).
63. A. Thibodeau, A. Erglu, C. S. McGinnis, N. Lawlor, D. Nehar-Belaid, R. Kursawe, R. Marches, D. N. Conrad, G. A. Kuchel, Z. J. Gartner, J. Banchereau, M. L. Stitzel, A. E. Cicek, D. Ucar, AMULET: A novel read count-based method for effective multiplet detection from single nucleus ATAC-seq data. *Genome Biol.* **22**, 252 (2021).
64. M. D. Young, S. Behjati, SoupX removes ambient RNA contamination from droplet-based single-cell RNA sequencing data. *Gigascience* **9**, gaa151 (2020).
65. C. S. McGinnis, L. M. Murrow, Z. J. Gartner, DoubletFinder: Doublet detection in single-cell RNA sequencing data using artificial nearest neighbors. *Cell Syst.* **8**, 329–337.e4 (2019).

66. J. A. Castro-Mondragon, R. Riudavets-Puig, I. Rauluseviciute, R. Berhanu Lemma, L. Turchi, R. Blanc-Mathieu, J. Lucas, P. Boddie, A. Khan, N. Manosalva Pérez, O. Fornes, T. Y. Leung, A. Aguirre, F. Hammal, D. Schmelter, D. Baranasic, B. Ballester, A. Sandelin, B. Lenhard, K. Vandepoele, W. W. Wasserman, F. Parcy, A. Mathelier, JASPAR 2022: The 9th release of the open-access database of transcription factor binding profiles. *Nucleic Acids Res.* **50**, D165–D173 (2022).
67. L. Haghverdi, A. T. L. Lun, M. D. Morgan, J. C. Marioni, Batch effects in single-cell RNA-sequencing data are corrected by matching mutual nearest neighbors. *Nat. Biotechnol.* **36**, 421–427 (2018).
68. J. T. Robinson, H. Thorvaldsdóttir, W. Winckler, M. Guttman, E. S. Lander, G. Getz, J. P. Mesirov, Integrative genomics viewer. *Nat. Biotechnol.* **29**, 24–26 (2011).
69. G. Yu, L.-G. Wang, Q.-Y. He, ChIPseeker: An R/Bioconductor package for ChIP peak annotation, comparison and visualization. *Bioinformatics* **31**, 2382–2383 (2015).
70. A. Subramanian, P. Tamayo, V. K. Mootha, S. Mukherjee, B. L. Ebert, M. A. Gillette, A. Paulovich, S. L. Pomeroy, T. R. Golub, E. S. Lander, J. P. Mesirov, Gene set enrichment analysis: A knowledge-based approach for interpreting genome-wide expression profiles. *Proc. Natl. Acad. Sci. U.S.A.* **102**, 15545–15550 (2005).
71. M. Ashburner, C. A. Ball, J. A. Blake, D. Botstein, H. Butler, J. M. Cherry, A. P. Davis, K. Dolinski, S. S. Dwight, J. T. Eppig, M. A. Harris, D. P. Hill, L. Isbel-Tarver, A. Kasarskis, S. Lewis, J. C. Matese, J. E. Richardson, M. Ringwald, G. M. Rubin, G. Sherlock, Gene Ontology: Tool for the unification of biology. *Nat. Genet.* **25**, 25–29 (2000).
72. G. O. Consortium, S. A. Aleksander, J. Balhoff, S. Carbon, J. M. Cherry, H. J. Drabkin, D. Ebert, M. Feuermann, P. Gaudet, N. L. Harris, D. P. Hill, R. Lee, H. Mi, S. Moxon, C. J. Mungall, A. Muruganugan, T. Mushayahama, P. W. Sternberg, P. D. Thomas, K. Van Auken, J. Ramsey, D. A. Siegele, R. L. Chisholm, P. Fey, M. C. Aspmontone, M. V. Nugnes, F. Quaglia, S. Tosatto, M. Giglio, S. Nadendla, G. Antonazzo, H. Attrill, G. Dos Santos, S. Marygold, V. Strelets, C. J. Tabone, J. Thurmond, P. Zhou, S. H. Ahmed, P. Asanithong, D. Luna Buitrago, M. N. Erdol, M. C. Gage, M. Ali Kadhum, K. Y. C. Li, M. Long, A. Michalak, A. Pesala, A. Pritazahra, S. C. C. Saverimutlu, R. Su, K. E. Thurlow, R. C. Lovering, C. Logie, S. Olierenko, J. Blake, K. Christie, L. Corbani, M. E. Dolan, H. J. Drabkin, D. P. Hill, L. Ni, D. Sitnikov, C. Smith, A. Cuzick, J. Seager, L. Cooper, J. Elser, P. Jaiswal, P. Gupta, P. Jaiswal, S. Naithani, M. Lera-Ramirez, K. Rutherford, V. Wood, J. L. De Pons, M. R. Dwinell, G. T. Hayman, M. L. Kaldunski, A. E. Kwitek, S. J. F. Laulederkind, M. A. Tutaj, M. Vedi, S.-J. Wang, P. D'Eustachio, L. Aimo, K. Axelsen, A. Bridge, N. Hyka-Nouspikel, A. Morgat, S. A. Aleksander, J. M. Cherry, S. R. Engel, K. Karra, S. R. Miyasato, R. S. Nash, M. S. Skrzypek, S. Weng, E. D. Wong, E. Bakker, T. Z. Berardini, L. Reiser, A. Auchincloss, K. Axelsen, G. Argoud-Puy, M.-C. Blatter, E. Boutet, L. Breuza, A. Bridge, C. Casals-Casas, E. Couder, A. Estreicher, M. Livia Famiglietti, M. Feuermann, A. Gos, N. Gruaz-Gumowski, C. Hulo, N. Hyka-Nouspikel, F. Jungo, P. Le Mercier, D. Lieberherr, P. Masson, A. Morgat, I. Pedruzzi, L. Pourcel, S. Pouy, C. Rivoire, S. Sundaram, A. Bateman, E. Bowler-Barnett, H. Bye-A-Jee, P. Denny, A. Ignatchenko, R. Ishraq, A. Lock, Y. Lussi, M. Magrane, M. J. Martin, S. Orchard, P. Raposo, E. Speretta, N. Tyagi, K. Warner, R. Zaru, A. D. Diehl, R. Lee, J. Chan, S. Diamantakis, D. Raciti, M. Zarowiecki, M. Fisher, C. James-Zorn, V. Ponferrada, A. Zorn, S. Ramachandran, L. Ruzicka, M. Westerfield, The Gene Ontology knowledgebase in 2023. *Genetics* **224**, iyad031 (2023).

#### Acknowledgments

**Funding:** This work was supported by NIDDK UC2DK126024, 2R01DK103740, and 1U54DK137332 (B.D.H.). Additional support was from the Japan Society for the Promotion of Science Postdoctoral Fellowships for Research Abroad, the Osamu Hayaishi Memorial Scholarship for Study Abroad, and the American Society of Nephrology Carl W. Gottschalk Research Scholar Award (Y.M.). **Author contributions:** Conceptualization: B.D.H. Library preparation: E.E.D. and Y.Y. Computational analysis: Y.M., N.L., and H.W. Experiment: Y.M., E.E.D., Y.Y., N.L., and Y.K. Online tool: H.W. Supervision: B.D.H. Writing: Y.M. and B.D.H.

**Competing interests:** B.D.H. is a consultant for Janssen Research & Development LLC, Pfizer, and Chinook Therapeutics, holds equity in Chinook Therapeutics, and has grant funding from Chinook Therapeutics and Janssen Research & Development. Y.Y. is currently an employee of Chugai Pharmaceutical Co. Ltd. The other authors declare that they have no competing interests. **Data and materials availability:** All data needed to evaluate the conclusions in the paper are present in the paper and/or the Supplementary Materials. The sequencing data generated in this study have been deposited in the GEO database under accession code GSE252111. The computational preprocessing and analytic codes for the single-nucleus data are available at Zenodo under record number 11522227 (v1). Previously published snRNA-seq data for mouse kidneys we analyzed in the paper are available in GEO (GSE139107). Previously published bulk RNA-seq data for human PTCs with siCREBS treatment are available in GEO (GSE220289). Gene expression, ATAC peaks, and gene activities for each cell type are also available via our interactive website Kidney Interactive Transcriptomics (<http://humphreyslab.com/SingleCell/>).

Submitted 25 January 2024

Accepted 28 June 2024

Published 7 August 2024

10.1126/sciadv.ado2849